CHRFAM7A diversifies human immune adaption through Ca^{2+} signalling and actin cytoskeleton reorganization

Kinga Szigeti,[a,*] Ivanna Ihnatovych,[a] Emily Notari,[a] Ryu P. Dorn,[a] Ivan Maly,[a] Muye He,[a] Barbara Birkaya,[a] Shreyas Prasad,[a] Robin Schwartz Byrne,[a] Dinesh C. Indurthi,[a] Erik Nimmer,[a] Yuna Heo,[a] Kolos Retfalvi,[a] Lee Chaves,[a] Norbert Sule,[b] Wilma A. Hofmann,[a] Anthony Auerbach,[a] Gregory Wilding,[a] Yongho Bae,[a] and Jessica Reynolds[a]

[a]State University of New York at Buffalo, 875 Ellicott St., Buffalo, NY, 14203, USA
[b]Roswell Park Comprehensive Cancer Center, 665 Elm St, Buffalo, NY, 14203, USA

eBioMedicine
2024;103: 105093
Published Online xxx
https://doi.org/10.1016/j.ebiom.2024.105093

Summary

Background Human restricted genes contribute to human specific traits in the immune system. *CHRFAM7A*, a uniquely human fusion gene, is a negative regulator of the α7 nicotinic acetylcholine receptor (α7 nAChR), the highest Ca^{2+} conductor of the ACh receptors implicated in innate immunity. Understanding the mechanism of how CHRFAM7A affects the immune system remains unexplored.

Methods Two model systems are used, human induced pluripotent stem cells (iPSC) and human primary monocytes, to characterize α7 nAChR function, Ca^{2+} dynamics and decoders to elucidate the pathway from receptor to phenotype.

Findings CHRFAM7A/α7 nAChR is identified as a hypomorphic receptor with mitigated Ca^{2+} influx and prolonged channel closed state. This shifts the Ca^{2+} reservoir from the extracellular space to the endoplasmic reticulum (ER) leading to Ca^{2+} dynamic changes. Ca^{2+} decoder small GTPase Rac1 is then activated, reorganizing the actin cytoskeleton. Observed actin mediated phenotypes include cellular adhesion, motility, phagocytosis and tissue mechanosensation.

Interpretation *CHRFAM7A* introduces an additional, human specific, layer to Ca^{2+} regulation leading to an innate immune gain of function. Through the actin cytoskeleton it drives adaptation to the mechanical properties of the tissue environment leading to an ability to invade previously immune restricted niches. Human genetic diversity predicts profound translational significance as its understanding builds the foundation for successful treatments for infectious diseases, sepsis, and cancer metastasis.

Funding This work is supported in part by the Community Foundation for Greater Buffalo (Kinga Szigeti) and in part by NIH grant R01HL163168 (Yongho Bae).

Keywords: Human immune diversity; CHRFAM7A; Ca^{2+} signalling; Actin cytoskeleton; Adaptation to the mechanical properties; Translational significance

Introduction

Considerable attention has been focused on the identification of duplicate genes that have emerged since the human-chimpanzee divergence, due to their potential to contribute to human-specific traits.[1] *CHRFAM7A*, a uniquely human fusion gene between *CHRNA7* and *FAM7A/ULK4*, is a negative regulator of the α7 nAChR function.[2]

α7 nAChR is highly expressed in the central and peripheral nervous system and in non-neuronal tissue.[3–6] In the immune system, it is detected in most cell types including innate and adaptive immunity.[7] α7 nAChR has been implicated in innate immunity and as part of the cholinergic anti-inflammatory response.[8,9] CHRFAM7A is abundantly expressed in the monocyte/macrophage lineage[10–13] and its role in the immune system is being investigated.[14,15] Overexpression of CHRFAM7A in murine macrophages resulted in decreased anti-inflammatory effect of α7 nAChRs and the receptor was retained in the ER.[16]

CHRFAM7A has two alleles, direct and inverted.[2,14,17] Genotypes are defined by a combination of copy number (0–4) and orientation of the gene.[14,17] 25% of the human population is homozygous for the direct, 25% is homozygous for the inverted and 50% is heterozygous

*Corresponding author.
E-mail address: szigeti@buffalo.edu (K. Szigeti).

Research in context

Evidence before this study

Human restricted genes that emerged after the human-chimpanzee divergence contribute to human specific traits, affecting fundamental processes in the brain, immune system, and metabolism. *CHRFAM7A*, a fusion gene between *CHRNA7* and *ULK4*, is incorporated into the α7 nAChR pentamer leading to a hypomorphic inotropic receptor. How this affects immune phenotypes had limited understanding and mechanistic insights were lacking.

Added value of this study

We demonstrate an innate immune gain of function that is specific to humans. The receptor to phenotype pathway is uncovered, indicating a hypomorphic receptor that changes Ca^{2+} signalling, the most ancient and central system in signal transduction affecting cell biology. We identify Rac1 as the Ca^{2+} decoder for actin cytoskeleton reorganization leading to more efficient monocytes that can invade previously immune restricted niches.

Implications of all the available evidence

Fundamental differences between human and rodent immunology lead to a translational gap when developing treatments for infectious and autoimmune diseases and metastatic cancer. Our work highlights one of these differences inferred by a human restricted gene and elucidates the pathway to identify druggable targets. Importantly, the divergence introduced by *CHRFAM7A* is not only human specific, but it also splits the human population 75%–25% for translated, direct allele *CHRFAM7A* carriers. Genetic heterogeneity represented by *CHRFAM7A* alleles needs to be considered for successful drug development relevant to the pathway.

carrying both direct and inverted alleles.[17] While *CHRFAM7A* is absent in 0.7% of the human population, these individuals are phenotypically normal.[17] The direct allele is translated, which leads to hypomorphic (decreased function) α7/CHRFAM7A nAChR.[12,13,17–21] On the other hand, the inverted allele is predicted to be non-translated and does not appear to influence α7 nAChR ionotropic function.[2,17]

CHRFAM7A can substitute 1–3 subunits in the α7 nAChR homopentamer forming the α7/CHRFAM7A nAChR, which is then transported to the plasma membrane (PM).[21,22] As an ionotropic receptor, α7/CHRFAM7A nAChR is hypomorphic, with decreased PM channel open probability.[20,21,23,24] α7 nAChR is implicated in Ca^{2+} signalling by contributing to the balance between calcium-induced calcium release (CICR) through its high Ca^{2+} conductance from the extracellular space (ionotropic α7 nAChR function) and inositol 1,4,5-trisphosphate IP3-induced calcium release (IICR) from the endoplasmic reticulum (ER) (metabotropic α7 nAChR function).[25–27] Overexpression of CHRFAM7A in human neuroblastoma SH-SY5Y cell line negatively regulates α7 nAChR, including intracellular Ca^{2+} concentration and neurotransmitter release.[28] Just recently we have demonstrated that CHRFAM7A modulates intracellular Ca^{2+} dynamics in neuronal cells as it shifts time spent in CICR to IICR.[29]

To decipher the specific mechanism of CHRFAM7A effect on α7 nAChR function in the innate immune system, we use a human isogenic iPSC model[17] and primary human monocytes (30 donors).

Methods

Ethics

The Institutional Review Board of the University at Buffalo, State University of New York approved the study. The informed consents were obtained from the donors.

Human primary monocytes

Source of primary human monocytes

Healthy volunteers meeting inclusion and exclusion criteria signed the informed consent. Inclusion criteria include healthy adult males and females between the ages of 20–55. Exclusion criteria include chronic, autoimmune or systemic inflammatory disease (rheumatoid arthritis, systemic lupus, myositis, inflammatory bowel disease, type 1 diabetes, autoimmune thyroiditis), use of NSAID within 48 h of blood draw, immunosuppressant medication use, any concurrent immune based therapies, fever within 36 h of blood draw, steroid use for any reason, anticoagulation or antiplatelet therapy, history of bleeding disorder, history of immune deficiency, pregnancy or treatment for cancer, blood donation within the 6 weeks prior to blood draw and use of illegal recreational drugs. Each donor provided up to 60 ml blood which was processed immediately for PBMC isolation. Yield of PBMC was quantified by cell counting and viability recorded. Sample was further processed for monocyte isolation if the viable PBMC was at least 500,000. Due to high human variance of monocyte percentage in humans, the number of monocytes ranged from 20,000 to 1,750,000. The available amount was prioritized in the following order: DNA isolation/genotyping, RNA isolation/qPCR, ICC and morphological analysis, Ca^{2+} imaging, migration and invasion assay.

Isolation of primary human monocytes

Peripheral blood was obtained from healthy adults with informed consent, and peripheral blood mononuclear cells were isolated by density gradient centrifugation using SepMate™ PBMC Isolation Tubes (Stem Cell

Technologies, Vancouver, Canada) and LymphoPrep (1.077 g ml^{-1}; Stem Cell Technologies, Vancouver, Canada) according to the manufacturer's instructions. Human primary monocytes were further isolated from the peripheral blood mononuclear cells using the Dynabeads® Untouched™ human Monocytes kit from Invitrogen (Carlsbad, CA, USA) according to the manufacturer's protocol.

Isogenic cell lines generation and culturing

UB068 (null) iPSC generated from human skin fibroblasts by episomal transformation were described previously.[17,18] UB068 was genome edited using TALENs to create isogenic, UB068_CHRFAM7A (direct) and UB068_CHRFAM7AΔ2bp (inverted) iPSC lines.[17] All iPSC lines were characterized for the expression of the pluripotency markers and the markers of the three germ-layer differentiation (Scorecard™ (Thermo Fisher) and ICC). For the isogenic lines, individual colonies were picked, PCR screened for the insertion, and passaged. Breakpoint specific TaqMan assay and RT-qPCR were used to quantify copy number and expression level of the inserted gene. Whole genome sequencing confirmed transgene insertion and excluded off target mutations.

iPSCs were grown on irradiated mouse embryonic fibroblasts in DMEM/F12-Glutamax medium supplemented with 10% KnockOut Serum Replacement, 1% Non-essential Amino Acids (NEAA), and 0.1% 2-Mercaptoethanol (all Thermo Fisher). Cells were maintained at 37 °C/5% CO2 and subcultured every 4–6 days using Dispase (Thermo Fisher).

Monocyte differentiation

Monocytes/macrophages were differentiated according to a well-established protocol.[30] Briefly, monocytes differentiation started with the iPSC detachment (at least two confluent 6-well plates) and embryoid body (EB) formation (Supplementary Figure S1). At day 4, the EBs were plated in X-Vivo 15 ™ medium (Lonza) supplemented with IL-3 (25 ng/ml) and MCSF (50 ng/ml). Starting from day 15, the generated monocytes were harvested twice a week from the supernatant and filtered through a 70 μm mesh nylon strainer (Falcon). For further monocytes/macrophages maturation, the cells were attached and cultured in X-Vivo 15 ™ medium (Lonza) supplemented with MCSF (100 ng/ml).

Whole cell patch clamp

Whole-cell currents were recorded using an IonFlux 16 automated patchclamp system (Fluxion Biosciences, Alameda, CA) on 96-well IonFlux microfluidic ensemble plates that give a cumulative whole-cell current from up to 20 cells. Differentiated monocytes were resuspended in extracellular solution containing (in mM) 138 NaCl, 4 KCl, 1.8 CaCl2, 1 MgCl2, 5.6 glucose, and 10 HEPES, pH adjusted to 7.4 with NaOH. Cells were captured in the trapping wells with intracellular solution containing (in mM) 60 KCl, 70 KF, 15 NaCl, 5 HEPES, and 5 EGTA, pH adjusted to 7.2 using KOH. Cells clamped at –80 mV were exposed to a 2s application of ACh (30 μM) or ACh + PNU-120596 (positive allosteric modulator of α7-nAChR) at varying concentrations, followed by 90s wash between applications to allow recovery from desensitization. IonFlux software (ver.4.5) was used for cell capture, seal formation, compound application, and data acquisition. Data collected using sampling frequency of 10 kHz was analysed using IonFlux Data Analyzer v5.0. Peak currents were plotted as a function of concentration and fit with a sigmoidal dose–response curve with variable slope using GraphPad Prism 5 (GraphPad Software, Inc., SanDiego, CA).

Ca^{2+} imaging

50,000 monocytes were plated on 24-well plates in either X-Vivo 15 ™ medium (Lonza) (iPSC-derived monocytes) or in 10% FBS RPMI medium (isolated from human donors) supplemented with MCSF (100 ng/ml). 72 h after plating, the cells were loaded with 1 μg/ml Fluo-8 AM (AAT Bioquest, Sunnyvale, CA, USA) in recording medium (20 mm HEPES, 115 mm NaCl, 5.4 mm KCl, 0.8 mm MgCl2, 1.8 mm CaCl2 and 13.8 mm glucose-Dojindo) containing 0.02% Cremophor EL (Dojindo) and incubated for 20 min at 37 °C and 5% CO2. Cells are loaded with fluo-4 fluorescent calcium ion indicator (Sigma, St. Louis MO) according to the manufacturer's protocol and imaged on an inverted fluorescence microscope (Leica DMi8, Leica, Buffalo Grove IL) using a cooled CCD camera (SPOT RT Slider, Diagnostic Instruments, Sterling Heights, MI). The indicator fluorescence is acquired as a time-lapse sequence before and after stimulation. Photobleaching, while qualitatively minimal, is normalized out for the purpose of quantitative measurements, based on a parallel control experiment with the same fluorescence excitation and imaging parameters.

Ca^{2+} signal extraction

Calcium data were analysed in MATLAB software (Mathsoft, Natick, MA). Fluorescence time courses corresponding to individual active regions (cells) were extracted from image series (videos), using MIN1PIPE package.[31] MIN1PIPE is a computer vision algorithm for calcium indicator fluorescence signal extraction from video recordings of cells. The package code was adapted to handle the data format in our videos.

Ca^{2+} kinetics

Kinetic parameters of the cell calcium system that are most likely given the fluorescence time courses were inferred using CaBBI module[32] or VBA package.[33] VBA is a machine learning algorithm for biological time series data. CaBBI is an algorithm for Bayesian inference of cellular kinetic parameters from fluorescent

intracellular calcium indicator time series. The calcium dynamics representation in CaBBI was modified to include the Li-Rinzel kinetic model of endoplasmic reticulum-mediated autonomous calcium spikes[34,35] and the kinetic model of α7 nicotinic receptor.[36] The kinetic model consists of the classic Li-Rinzel model[34] capable of reproducing calcium oscillations with an addition of the kinetics of PM channel and pump currents.[36] Model parameters include:1) ER pump Vmax, measuring evacuation of calcium into the ER by SERCA; 2) InsPR k, measuring IP3-induced efflux from the ER; 3) ER leak k, measuring background efflux from the ER; 4) IP3 t, the lifetime of IP3; 5) IP3 (production) Vmax, measuring activity of phospholipase C; 6) PM influx, measuring the (constant) calcium current across the PM into the cytosol (which with respect to this dataset represents the ligand-independent current); 7); PM pump Vmax, measuring evacuation of calcium into the extracellular space by PMCA. Overall, the functionality of our computational pipeline is similar to that in a recent Bayesian analysis of calcium dynamics in a mammary epithelial cell line.[37]

Ca^{2+} cytoplasmic area quantification

Single cell Ca^{2+} area measurements were extracted from Ca^{2+} time lapse recordings. Ca^{2+} recordings were exported to FIJI ImageJ as a single cell image and multiple time-series images corresponding to pre-treatment and post-treatment recordings. Ca^{2+} areas for each cell were quantified before drug treatment and after drug treatment. The pre-treatment and post-treatment area measurements were then compared using a dependent two-tailed t-test.

First, the cell image was binarized. Watershed was used to segment overlapping cells. Then the analyse particles plugin was used to outline the binary image. These outlines were recorded as regions of interests (ROIs) for the next step of the analysis. Second, time series images were background subtracted using the first frame of each time series. The resulting time series depicted changes in intracellular calcium. Z project was then used to collapse the time series into a single image containing the average intensity of the intracellular calcium activity. This average intensity image was then binarized with an intensity threshold of 10. Next, ROIs from the cell image were overlayed onto the binarized average intensity Ca^{2+} image. Finally, the ROIs were measured, and the resulting area measurements were recorded for before treatment and post treatment conditions.

Directionality analysis

Fluorescence time courses corresponding to individual active regions (cells) were extracted from image series (videos). Randomly selected 50 cells (Regions of interest; ROI) were processed through ImageJ directionality analysis resulting in directionality and dispersion (Fourier components) dataset obtained from 60 images times 50 cells (3000 images) in each cell line. Distribution of dispersion was compared by Kolmogorov–Smirnov (KS) statistics and distributions were plotted in R. Single cell directionality analysis is depicted as montage of the Fourier directionality video.

Primary monocytes from human donors were isolated and Ca imaged as described above. 600 images per donor was analysed for dispersion (Fourier components). Comparison of distribution between genotype groups was performed by KS statistics and distributions were plotted in R. Single cell directionality analysis by Local Gradient Orientation (LGO) is depicted at single cell level. Single cell directionality histograms are generated by Fourier component directionality.

Flow cytometry

Approximately 0.5×10^6 cells were blocked with True-Stain monocyte blocker (Biolegend) in 0.1 ml FACS buffer for 5 min on ice. Fluorescently labelled antibodies (Supplementary Table S5) were directly added and allowed to stain on ice for an additional 30 min. Cells were washed with 1 ml FACS buffer, resuspended in 0.5 ml FACS buffer and analysed on a BD LSR-Fortessa flow cytometer. Fluorescence minus one (FMO) controls were stained in parallel to establish proper gating. Data were analysed using FlowJo software (https://www.flowjo.com/).

qPCR

Total RNA was isolated using Trizol (Invitrogen) according to manufacturer's protocol. cDNA was synthesized from 500 ng RNA using iScript™ cDNA Synthesis Kit (Bio-Rad). Quantitative gene expression was detected by standard RT-qPCR using specific primers listed in Supplementary Table S4 with either SYBR green master mix (Biotool) or TaqMan (Thermo Fisher) run on Bio-Rad CFX Connect cycler (Bio-Rad). Relative gene expression was quantified by ΔΔCT method normalized to GAPDH expression assayed with 3 technical replicates. Data are presented as the average of the triplicates ± standard error of the mean.

ICC

Monocytes plated on glass coverslips or 8-well glass chambers (Thermo Fisher) were fixed with 4% paraformaldehyde (Mallinckrodt Baker) for 15 min, permeabilized with 0.1% Triton ×100 (Mallinckrodt Baker) for 10 min and blocked with blocking buffer (5% BSA in PBS) for 1 h at room temperature (RT). Cells were incubated overnight at 4 °C with primary antibodies listed in Supplementary Table S5 and for 1 h at RT with secondary antibodies. Both primary and secondary antibodies were diluted in blocking buffer. Slides/coverslips were incubated with NucBlue (DAPI) for 5 min at RT and mounted with a ProLong® Gold Antifade reagent (Life Technologies). Confocal images were captured by using Leica TCS SP8 confocal microscope

system (63× and/or 20× objective). Images were acquired using Leica Application Suite (LAS X) software.

ELISA

Following isogenic macrophages treatment with LPS, media were collected and stored at –80 °C. The concentration of IL-6 in the cell culture media was quantified using IL-6 ELISA kit (R&D Systems) according to the manufacturer's protocol.

Hydrogels

Fibronectin-coated polyacrylamide hydrogels were prepared as previously described.[38] The acrylamide concentration remained constant at 7.5% while the bisacrylamide concentration were 0.03% (2–4 kPa) and 0.06% (4–8 kPa) for soft hydrogels, 0.15% (10–12 kPa) and 0.3% (22–24 kPa) for intermediate stiffness hydrogels and 0.6% (over 30 kPa) for stiff hydrogels.

Morphological analysis with ImageJ

Morphological analysis in FIJI was conducted using built-in segmentation features. Images obtained of iPSC-derived monocytes on 0.03–0.6 stiffness hydrogels were captured using EVOS FL fluorescent microscope (20× objective). Fluorescent images were split into RGB channels whereby green channel (cell body) images were converted into binary format and fine-tuned to avoid segmentation of overlapping cells and incomplete images. FIJI generated cell outlines were used to verify monocyte count and segmentation. Values of circularity (4π*area/perimeter2), solidity (area/convex area), and perimeter were used to identify differences in cell morphology. Subsequent statistical analysis was conducted in R-Studio.

G-LISA

Activity of small GTPases (CDC42, Rac1, and RhoA) in the monocytes derived from the null, direct, and inverted iPSC lines was measured by G-LISA Activation Assay (Cytoskeleton Inc.) according to the manufacturer's protocol. The monocytes derived from the three lines were starved overnight, collected by centrifugation (300 x g, 4 min, RT), plated on 0.15% hydrogels and incubated at 37 °C for 30 min (with or without pharmacological treatment). Afterwards, the cells were lysed with an appropriate lysis buffer and centrifugated (10,000 x g, 1min, 4 °C). Supernatants were immediately frozen and kept at –80 °C till the G-LISA Activity Assay. Protein concentration was measured by Precision Red™ Advanced Protein Assay (Cytoskeleton Inc.).

Pharmacological modulation of small GTPases

Activity of small GTPases were modulated by the specific inhibitors: ML 141 (CDC42), EHT 1864 (Rac1), and Rhosin (RhoA). Monocytes (5×10^5–1×10^6 cells) derived from the three lines were resuspended in the plain X-Vivo 15™ medium (Lonza) containing 10 μM of a specific GTPase inhibitor, plated on 0.15% hydrogels and incubated at 37 °C for 30 min. The cells were collected as described above and subjected to the specific G-LISA Activation Assay.

Atomic force microscopy

Atomic force microscopy (AFM) was used to measure intracellular stiffness.[39] iPSC-derived monocytes (null, direct, and inverted) were plated on low (0.03), intermediate (0.15), and stiff (0.6) polyacrylamide hydrogels for 1 h and were indented using a silicon nitride cantilever (Asylum, BL-AC40TS-C2; spring constant, 0.05–0.12 N/m) with a three-sided pyramidal AFM tip (8 nm in radius). The stiffness of each cell was measured using AFM in contact mode using an NX12 AFM system (Park Systems) mounted on a Nikon ECLIPSE Ti2 inverted microscope. To analyse the stiffness, the first 400 nm of horizontal tip deflection was fitted with the Hertz model for a three-sided pyramid and a 35° face angle to determine intracellular stiffness. For each experimental condition, 3 force curves per cell were acquired for a total of 10 cells. AFM experiments were independently repeated three times (obtaining a total of 90 force curves for each cell type per experimental condition). Using AFM analysis software XEI (Park Systems), the force curves were quantified and converted to Young's modulus (stiffness).

Migration and invasion assay

Migration and invasion properties of the iPSC-derived and PBMC-derived monocytes were assessed using CHEMICON® QCM™ 24-well Migration Assay Kit (MilliporeSigma) according to the manufacturer's instructions. 200,000 cells were plated in the upper chamber of the insert with an 8 μm pore size and allowed to migrate for 16 h. CXCL12 (100 ng/ml) was used as a chemoattractant. Migration was detected colorimetrically. To assess invasive characteristics of the monocytes, the inserts were coated for 1 h with Matrigel (Corning) prior to the assay.

Adhesion assay

Adhesive properties of the UB068 and UB068_CHRFAM7A derived monocytes were quantified according to.[40] Briefly, 96-well plates were coated for 1 h, 37 °C with 10 μg/ml of either truncated laminin (Takara Bio) or Geltrex (Thermo Fisher) and blocked for 1 h, RT with 0.5% BSA/PBS. Afterwards, 20,000 monocytes/well (in quadruplicates) were seeded and incubated for 30 min at 37 °C, then fixed with 4% PFA/PBS and stained with Crystal Violet. Adhesion was quantified colorimetrically as absorption at 550 nm.

Phagocytosis

In vivo phagocytosis in iPSC-derived macrophages grown on glass coverslips was detected using 1 μm polystyrene yellow-green FluoSpheres (Themo Fisher)

as described in.[41] A total of 5 μL of FluoSpheres was directly added to macrophage maturation media (10^7 beads/mL/10^5 cells) and incubated for four different time intervals (0.5 h, 1 h, 2 h, and 4 h). After incubation, the cells were washed twice with PBS, fixed with 4% PFA/PBS and imaged using EVOS FL fluorescent microscope (40× objective). 10–15 images/time point/cell line were taken and analysed by two raters in three independent experiments.

Gelatine degradation

Gelatine degradation assay was performed according to.[42] Briefly, 12 mm glass coverslips were coated with Oregon Green-488 gelatine (0.2% w/v in PBS) as described.[42] 25,000 iPSC-derived monocytes were collected by centrifugation at 300 x g, 4 min, RT and plated on the gelatine coated coverslips for 3 h, 16 h, or 48 h. Afterwards, the coverslips were fixed with 4% PFA and the cells were stained with 555-Actin (Thermo Fisher). Nuclei were counterstained with NucBlue (Thermo Fisher). The images were taken on EVOS-FL fluorescent microscope (Thermo Fisher) using 20× and 40× objectives.

Statistical analysis

Experiments in the iPSC model system were performed in duplicates or triplicates. Values are expressed as mean ± SD or ±95% CI as indicated in the figure legends. In box plots, outlying points are plotted when values that are further the distance of 1.5*IQR starting from upper/lower hinge (<Q1—1.5*IQR or > Q3 + 1.5*IQR). Statistical comparisons with regards to continuous variables were applied using the independent two-tailed t-test (for comparisons between two groups), Mann–Whitney U Test (for nonparametric comparisons between two groups), Wilcoxon signed-rank test (for paired samples), and two-way ANOVA (for comparisons among three or more groups). Diagnostic plots were used to assess model assumptions associated with testing procedures. Comparisons between cumulative density functions were applied by the nonparametric two-sample Kolmogorov–Smirnov test. To control for Type I error rates due to multiple testing, Bonferroni correction was implemented in our comparisons. All statistical analyses were performed using R software package (version 4.1.2) and GraphPad Prism (version 10.1.0).

Role of funders

Funders did not have any role in study design, data collection, data analyses, interpretation, or writing of report.

Results

Isogenic iPSC model of CHRFAM7A alleles

Isogenic *CHRFAM7A* iPSC model was described previously.[17] iPSC were differentiated into monocytes using an established protocol (Supplementary Fig. S1a).[30] Monocytes were characterized by flow cytometry for negative (CD3, CD19, CD66, CD56) and positive (CD14, CD16, MHCII, CD86) markers (Supplementary Fig. S1b), Giemsa stain and CD68 immunocytochemistry (ICC) (Supplementary Fig. S1c). Cytokine expression and release (Supplementary Fig. S1d and e) confirmed functional monocytes.

Primary human monocytes genotyped for CHRFAM7A alleles

Monocytes were isolated from 30 healthy human donors (Supplementary Table S1) between the ages of 18–55 after IRB approval and informed consent.[43] Donors were genotyped for copy number and orientation of *CHRFAM7A* alleles.[17] Genotype distribution in the cohort is 20% homozygous direct, 33% homozygous inverted and 47% heterozygous. Due to variability of monocyte proportion in human white blood cells (1–22%) and the number of cells needed for each assay, we established a stepwise protocol of primary monocyte utilization. ICC with phalloidin and morphological analysis was performed on all donors (6 Direct (D), 10 Inverted (I), 14 Heterozygous (HZ)). Ca^{2+} imaging was executed on 16 samples (3D, 5I, 8HZ), migration and/or invasion assay on 14 samples (3D, 4I, 7HZ).

CHRFAM7A modifies the α7 nAChR into a hypomorphic ionotropic receptor in isogenic iPSC derived monocytes

In humans, CHRFAM7A incorporates into the α7 nAChR.[22] We and others have demonstrated that the presence of CHRFAM7A leads to a hypomorphic plasma membrane receptor,[17,18] with decreased α-bungarotoxin (BGT) and amyloid beta binding.[44,45] In contrast, α7 nAChR function is not affected by the presence of the inverted allele in the neuronal lineage.[17]

The data about ionotropic properties of α7 nAChR in human immune cells is inconsistent and requires further investigation. While originally α7 nAChR macroscopic currents were not detected in non-excitable cells,[11,46] recent reports utilizing whole cell patch clamp with α7 nAChR selective agonists and allosteric modulators clearly demonstrated the presence of functionally active α7 nAChR in human PBMC-derived macrophages[47] and THP-1 macrophages.[48]

We performed electrophysiological studies using whole cell patch-clamp on iPSC derived monocytes in the presence of PNU 120596 (positive allosteric modulator of α7 nAChR) and demonstrated functional α7 nAChR. In all iPSC derived monocytes, UB068 (null), UB068_CHRFAM7A (direct) and UB068_CHRFAM7AΔ2bp (inverted), PNU 120596 and ACh responsive channel opening was detected. Null and inverted monocytes had similar currents (p-value for 1 and 10 mM PNU were 0.079 and 0.036, respectively, two-way ANOVA) while direct monocytes demonstrated

lower action potential indicating a hypomorphic receptor (p-value for 1 and 10 mM PNU were 0.0002 and 0.019, respectively, two-way ANOVA) (Fig. 1a and b). As α7 nAChR is the highest Ca^{2+} conductor among the nAChR,[25] we decided to methodologically move downstream, inside the cell, and measure intracellular Ca^{2+} dynamics in the context of *CHRFAM7A* alleles.

CHRFAM7A effect on Ca^{2+} dynamics in isogenic iPSC derived monocytes

Fluo-4 fluorescent Ca^{2+} imaging traces of individual cells were extracted and quantified utilizing an image analysis algorithm previously developed for neurons (MIN1PIPE)[31] (Fig. 1c and d). We detected spontaneous Ca^{2+} oscillations that demonstrated *CHRFAM7A* genotype specific distinct peak characteristics (Fig. 1d and e). Ca^{2+} dynamic curves in direct monocytes exhibited markedly lower amplitude compared to null ($p < 0.0001$, KS statistics), while in inverted monocytes Ca^{2+} traces were similar to null ($p = 0.0125$ for amplitude, $p = 0.0505$ for FWHM; $p = 0.976$ for frequency, KS statistics) (Fig. 1e).

CHRFAM7A allele specific modulation of CICR and IICR

We turned to AI based single cell analysis of genotype specific Ca^{2+} dynamics to elucidate the mechanism of Ca^{2+} signal regulation in the context of the direct and inverted *CHRFAM7A* alleles. Bayesian inference of kinetic parameters of the cell Ca^{2+} system was carried out by adapting the neuronal Ca^{2+} signal analysis algorithm CaBBI.[32] The kinetic model consists of the classic Li-Rinzel model[34] capable of reproducing Ca^{2+} oscillations with an addition of the kinetics of PM channel and

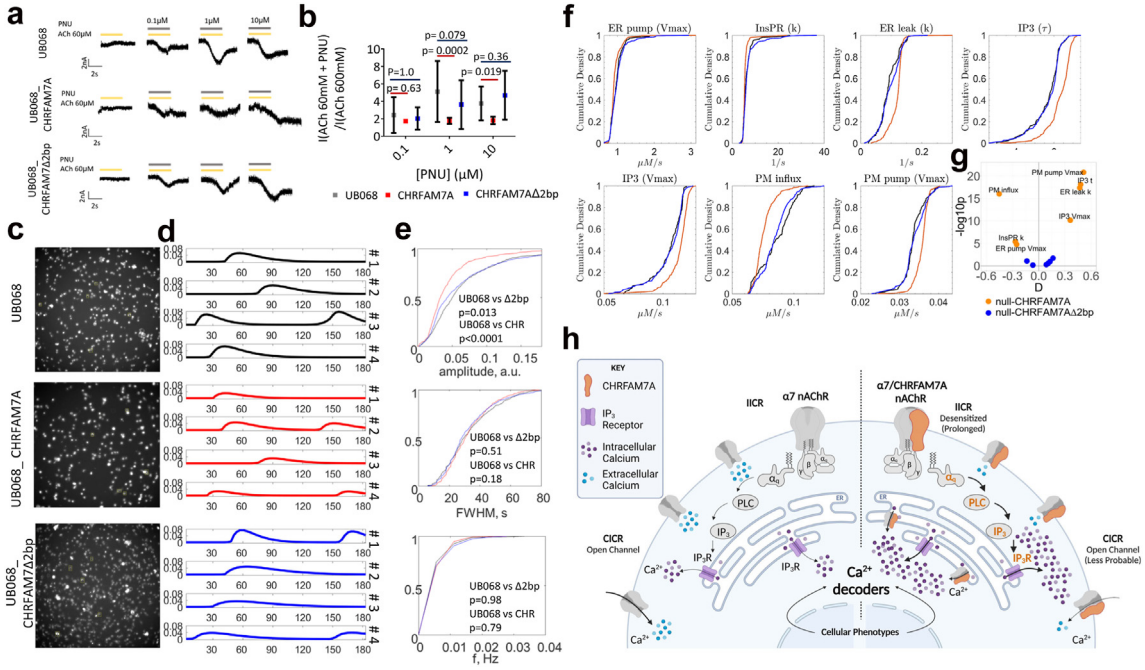

Fig. 1: **Electrophysiology and Ca^{2+} dynamics in UB068 (null), UB068_CHRFAM7A (direct) and UB068_CHRFAM7AΔ2bp (inverted) iPSC derived isogenic monocytes.** a. Whole-cell recordings on automated high-throughput patch-clamping system on iPSC derived isogenic monocytes. Application of ACh (60 mM) and co-application of PNU120596 with 60 mM ACh with increasing concentration of PNU120596. b. PNU120596 and ACh response fold change in iPSC derived isogenic monocytes. Represented as Mean ± 95% CI (N = 5, two-way ANOVA (Cell Line and [PNU]) and Bonferroni correction for multiple testing). c. Representative fluorescent images, ROI and d. Spontaneous Ca^{2+} oscillation traces of iPSC derived isogenic monocytes. e. Cumulative density curves of Ca^{2+} peak characteristics in UB068 (black), UB068_CHRFAM7A (red) and UB068_CHRFAM7AΔ2bp (blue) monocytes. Operator independent analysis of single cell Ca^{2+} tracings was performed in MatLab. (A amplitude, FWHM full width at half maximum amplitude, f frequency). (N = 3, 50–100 peaks per cell line, two-sample KS test and Bonferroni correction for multiple testing). f. Cumulative density plots of CaBBI inferred kinetic parameters of the spontaneous Ca^{2+} dynamic curves in UB068 (black), UB068_CHRFAM7A (red) and UB068_CHRFAM7AΔ2bp (blue) monocytes. (***ER pump Vmax***, Ca^{2+} reuptake into the ER by SERCA, ***InsPR k***, IP3-induced efflux from the ER, ***ER leak k***, background efflux from the ER, ***IP3 t***, the lifetime of IP3, ***IP3*** (production) ***Vmax***, activity of phospholipase C, ***PM influx***, (constant) Ca^{2+} current across the PM into the cytosol and ***PM pump Vmax***, evacuation of Ca^{2+} into the extracellular space by PMCA). g. The maximum distance between curves (D) and -log10p of two-sample KS test depicted in the adapted volcano plot (null-CHRFAM7A (orange) and null-CHRFAM7AΔ2bp (blue) comparison). (N = 3, 100 cells per cell line, two-sample KS test and Bonferroni correction for multiple testing). h. Proposed model of CHRFAM7A effect on Ca^{2+} dynamics (created with BioRender.com).

pump currents.[36] Model parameters include:1) ER pump Vmax, measuring evacuation of Ca^{2+} into the ER by SERCA; 2) InsPR k, measuring IP3-induced efflux from the ER; 3) ER leak k, measuring background efflux from the ER; 4) IP3 t, the lifetime of IP3; 5) IP3 (production) Vmax, measuring activity of PLC; 6) PM influx, measuring the (constant) Ca^{2+} current across the PM into the cytosol (which with respect to this dataset represents the ligand-independent current); 7); PM pump Vmax, measuring evacuation of Ca^{2+} into the extracellular space by PMCA. CaBBI analysis confirmed that the direct *CHRFAM7A* allele (UB068_CHRFAM7A) is associated with a hypomorphic receptor demonstrating lower Ca^{2+} influx rate across the PM ($p = 3 \times 10^{-13}$, Kolmogorov–Smirnov statistics) compared to null (UB068) cells[17,18,24] leading to decreased CICR activity (Fig. 1f and g). UB068_CHRFAM7A (direct) cells demonstrated increased lifetime of IP3 ($p = 4.97 \times 10^{-14}$, KS statistics) and increased activity of PLC ($p = 3.68 \times 10^{-7}$, KS statistics) consistent with increased IICR activity (Fig. 1f and g). These data align with the notion that the α7/CHRFAM7A nAChR is hypomorphic for PM channel mediated ionotropic function, shifting the receptor to the closed state where IICR is active.[49] Alternatively, prolonged closed state can be reached by receptor desensitization. While further work is needed to fully decipher the mechanism of the shift to the closed state, this closed state increases time spent in IICR. Interestingly, UB068_CHRFAM7A (direct) monocytes exhibited a higher background eflux from the ER ($p = 2.62 \times 10^{-16}$, KS statistics) suggesting increased ER leak (Fig. 1f and g). In contrast, CaBBI analysis of UB068_CHRFAM7AΔ2bp (inverted) monocytes is indistinguishable from the null (UB068) (Supplementary Table S2) (Fig. 1e and g).

Taken together with the patch clamp data, the effect of the direct allele on Ca^{2+} signalling is a distinct, α7 nAChR dependent mechanism that is different from null.[17,18] α7/CHRFAM7A nAChR shifts the reservoir for cytoplasmic Ca^{2+} influx from the extracellular space to the ER leading to cell autonomous Ca^{2+} oscillations. The proposed mechanism for the α7/CHRFAM7A nAChR mediated Ca^{2+} dynamics is depicted in Fig. 1h. Conversely, α7 nAChR electrophysiology and Ca^{2+} dynamics analysis of the inverted allele demonstrated that it is null from the α7 nAChR perspective. We proceeded to characterize Ca^{2+} dynamics of the α7/CHRFAM7A nAChR.

Ca^{2+} signalling by the α7/CHRFAM7A nAChR

Single cell cytoplasmic total Ca^{2+} pool was quantified from the Fluo-4 videos for the spontaneous Ca^{2+} oscillations and after pharmacological treatments with drugs affecting the proposed mechanism: α7 nAChR agonist acetylcholine (ACh), α7 nAChR antagonist α-bungarotoxin (BGT), SERCA inhibitor thapsigargin (TG), PLC inhibitor U73122, and IP3 receptor antagonist xestospongin (Xesto). Agonist and antagonist response (Fig. 2a black) increased and decreased the Ca^{2+} signal, respectively, as expected in the null line; α7/CHRFAM7A nAChR demonstrated a mitigated effect consistent with the hypomorphic receptor and possible decreased binding Fig. 2a orange).[44,45] TG significantly diminished Ca^{2+} signal after a brief transient increase by depleting the ER Ca^{2+} pool in both lines ($p < 0.0001$, Wilcoxon signed-rank). U73122 treatment increased the Ca^{2+} signal in null ($p = 0.0014$, Wilcoxon signed-rank) and CHRFAM7A (D) cells ($p < 0.0001$, Wilcoxon signed-rank), albeit it is higher in CHRFAM7A monocytes. More recent literature suggest that U73122 may not exert its effect through inhibition of PLCγ, rather it increases cytoplasmic Ca^{2+} steady state[50–52] and directly activates PLCβ2. Xesto decreased the Ca^{2+} signal in null monocytes as expected. CHRFAM7A monocytes demonstrated a paradoxical increase in the Ca^{2+} signal, which is explained by the complex mechanism of Xesto, including both blocking IP3 induced ER release and ER reuptake of cytoplasmic Ca^{2+}.[53] The paradoxical increase of the Ca^{2+} signal after Xesto treatment in CHRFAM7A monocytes suggest that the ER leak is facilitated by the reset of baseline cytoplasmic Ca^{2+} steady state and preservation of the ER Ca^{2+} pool.[50–53]

Single cell Ca^{2+} dynamics curves captured by the Fluo-4 videos demonstrated distinct pharmacological responses (Fig. 2b and d). α7 nAChR dependence was confirmed: ACh increased the amplitude in both null and CHRFAM7A monocytes. BGT decreased the amplitude in null monocytes as expected, while paradoxical increase in the amplitude in CHRFAM7A cells was noted. BGT being not membrane permeable isolates α7 nAChR PM and ER effects on Ca^{2+} dynamics. The increased BGT amplitude in CHRFAM7A monocytes is likely related to engaging the PM α7/CHRFAM7A nAChR in the channel-closed sate facilitating IICR. This phenomenon, the paradoxical increase in amplitude after BGT treatment, was present in CHRFAM7A carrier primary human monocytes as well, compared to the noncarriers (Fig. 2c).

Pharmacological modulation of the ER dependent aspects of the Ca^{2+} dynamics curve confirmed that depletion of the ER Ca^{2+} reservoir by TG decreased the width of the Ca^{2+} dynamic curve in both the null and CHRFAM7A monocytes (Fig. 2d). In contrast, preserving Ca^{2+} in the ER (U73122 and Xesto) increased amplitude in CHRFAM7A monocytes (Fig. 2d) implicating an IICR independent ER leak as an important contributor to the Ca^{2+} dynamics. Of note, CaBBI analysis also suggested the presence of IP3 receptor independent, enhanced ER leak (Fig. 1f and g), which raises the possibility of partial mislocalization of the α7/CHRFAM7A nAChR harbouring both wide type and mutant subunits (Fig. 2b and c). CHRFAM7A harbours a truncated and modified extracellular domain lacking two of the three glycosylation sites required for transport

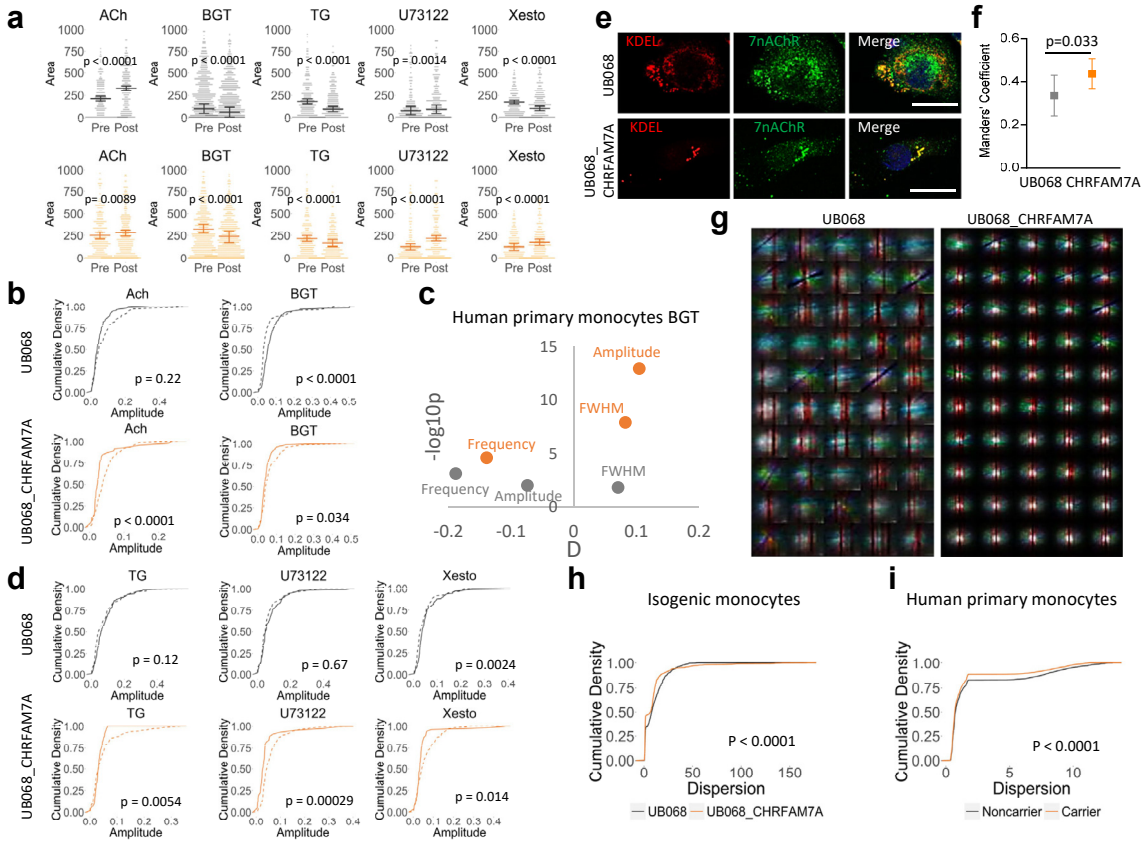

***Fig. 2:* Characterization of the α7/CHRFAM7A nAChR**. a. Pharmacological modulation of the cytoplasmic Ca^{2+} pool measured by change in Ca^{2+} signal before and after treatment with agonist acetylcholine (ACh), antagonist BGT, SERCA inhibitor TG, PLC inhibitor U73122, and IP3 receptor antagonist Xesto. Represented as Mean ± 95% CI (50–100 cells, Wilcoxon signed-rank test and Bonferroni correction for multiple testing). b. Agonist and antagonist effect on amplitude in UB068 and UB068_CHRFAM7A isogenic monocytes depicted as cumulative density curves (75–100 cells per cell line, two-sample KS test and Bonferroni correction for multiple testing). c. Maximum distance between curves (D) and -log10p of two-sample KS test depicted in the adapted volcano plot (null (gray), CHRFAM7A (orange)) of Ca^{2+} dynamics changes to BGT treatment in human primary monocytes (1147 noncarrier (black) and 2407 carrier (orange) peaks analysed from 15 donors) (FWHM full width at half maximum amplitude). d. Effect of ER pool depletion (TG) and PLC inhibitor U73122, and IP3 receptor antagonist Xesto on Ca^{2+} dynamics depicted as cumulative density curves. (N = 3, 50–100 peaks per cell line, two-sample KS test and Bonferroni correction for multiple testing). e. Representative confocal images of UB068 and UB068_CHRFAM7A isogenic macrophages stained with the α7/CHRFAM7A nAChR antibody (green) and ER marker KDEL (red); colocalization (orange). Scale bar, 10 μm. f. Mander's coefficient of colocalization (M1) of ER and α7/CHRFAM7A nAChR signal calculated in ImageJ. Represented as Mean ± SD (N = 3, 25–50 cells, independent two-tailed t-test). g. Representative single cell directionality montage (3 min sample) of Fourier analysis in UB068 and UB068_CHRFAM7A isogenic monocytes. Null (UB068) demonstrating multifocal Ca^{2+} flickers and CHRFAM7A (UB068_CHRFAM7A) showing monofocal, organized, robust Ca^{2+} signal originating from the ER. h. Cumulative distribution curves of Fourier dispersion parameter in UB068 (black) and UB068_CHRFAM7A (orange) isogenic monocytes. (N = 3, 1800 images per cell line, Two-sample KS statistics, Bonferroni corrected p-values. For visualization of the distribution plots data is truncated at 95th percentile). i. Cumulative distribution curves of Fourier dispersion parameter in noncarrier (black) and carrier (orange) primary human monocytes from 15 donors (5NC, 10C). (10 random, active cells form each donor representing 600 images, Two-sample KS statistics, Bonferroni corrected p-values. For visualization of the distribution plots data is truncated at 95th percentile).

to the plasma membrane.[54] ICC using ER marker (KDEL) and α7/CHRFAM7A nAChR antibody demonstrated co-occurrence of the signal, suggesting ER retention of α7/CHRFAM7A nAChR (Fig. 2e and f). The Manders' coefficient (M1) was calculated to quantify the amount of green signal (α7/CHRFAM7A nAChR) overlapped the red signal (KDEL) using ImageJ (https://imagej.net/ij).

Time-lapse video microscopy demonstrated the difference in intracellular distribution of the Ca^{2+} signal. The null displayed a multidirectional-multifocal flicker pattern consistent with PM mechanism, while CHRFAM7A monocytes displayed a unifocal-unidirectional robust Ca^{2+} signal originating centrally consistent with utilization of the ER Ca^{2+} reservoir (Fig. 2g). To quantify the observed difference, single cell

directionality analysis was performed to obtain Fourier dispersion spectra for each cell. Dispersion of Ca^{2+} signal of 50 cells in each line demonstrated a shift towards less dispersion in CHRFAM7A monocytes compared to null ($p < 0.0001$, KS statistics), an indication of a more localized signal (Fig. 2h). Genotype grouped cumulative distribution curves of Fourier dispersion parameter in carrier and noncarrier monocytes from 16 human donors confirmed that Ca^{2+} signal is less dispersed in carrier monocytes than in noncarriers ($p = 0.0001$, KS statistics) (Fig. 2i).

Preferred membrane structure

iPSC derived monocytes revealed striking morphological differences in preferred membrane structure/shape (Fig. 3a). The null line formed filopodia while CHRFAM7A monocytes developed lamellipodia (Fig. 3a). As membrane specialization is linked to actin dependent cytoskeletal dynamics,[55] we used fluorescent phalloidin staining and operator independent single cell analysis to quantify the morphological changes (using ImageJ/Fiji, Supplementary Fig. S2).[56] CHRFAM7A monocytes were less circular and had a larger perimeter compared to null (Fig. 3b). Primary human monocytes from 20 donors demonstrated the same shift in morphology between CHRFAM7A carriers and noncarriers as seen in the iPSC derived monocytes (Fig. 3c and d): carrier (C) monocytes are less circular and have larger perimeter than noncarrier (NC) primary monocytes. In the iPSC model the distinct membrane morphology was accompanied by activation of small Rho family GTPases in the expected pattern: CDC42 drives filopodia in null and Rac1 promotes lamellipodia formation in CHRFAM7A iPSC

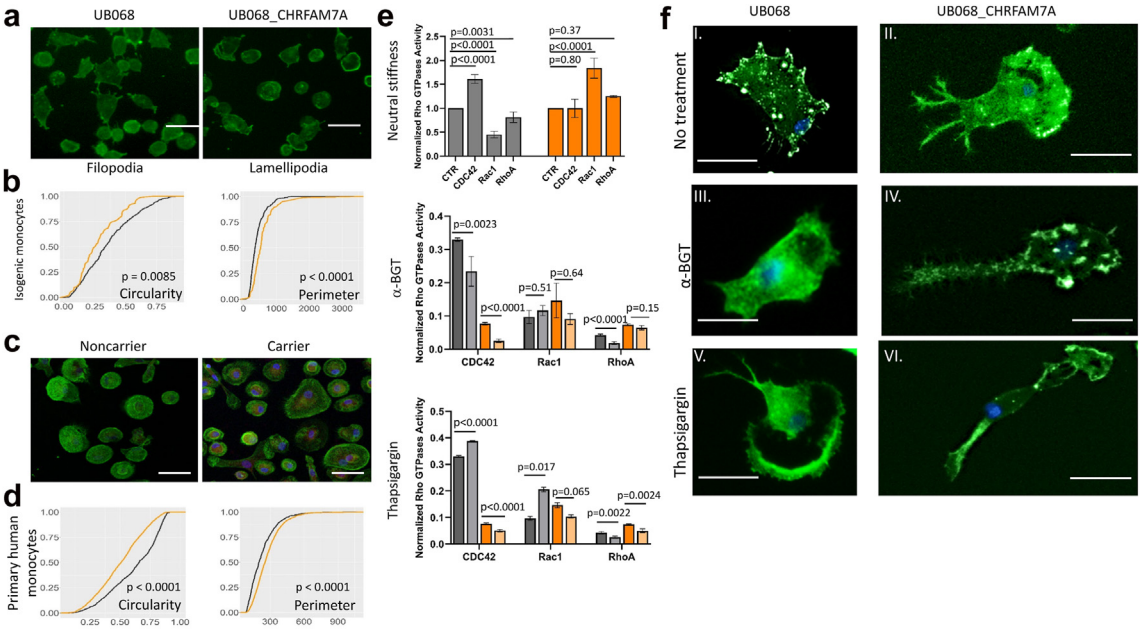

***Fig. 3:* CHRFAM7A associated cytoskeletal remodelling and preferred membrane structure**. a. Fluorescent phalloidin microscopy images of UB068 and UB068_CHRFAM7A isogenic monocytes plated on polyacrylamide hydrogels (0.15%) demonstrating filopodia in null and lamellipodia in CHRFAM7A monocytes. Scale bar, 50 µm. b. Operator independent morphological analysis (Fiji/Image J) of UB068 and UB068_CHRFAM7A isogenic monocytes. Cumulative density curves demonstrate shift in circularity and perimeter between null (black) and CHRFAM7A (orange) monocytes (Two-sample KS statistics, Bonferroni corrected p-values). c. Representative fluorescent phalloidin microscopy images of primary human monocytes from noncarrier and carrier donors. Scale bar, 50 µm d. Operator independent morphological analysis of primary human monocytes (10NC black, 20C orange) demonstrates similar shift in morphology as seen in the iPSC derived monocytes. Carrier monocytes have larger perimeter and are less circular compared to noncarrier monocytes (Two-sample KS statistics, p-values for CHRFAM7A and null comparison after Bonferroni multiple testing correction). e. G-LISA assay demonstrating activity of small GTPases CDC42, Rac1 and RhoA in UB068 (black) and UB068_CHRFAM7A (orange) non-treated isogenic monocytes (top panel). Data are presented as mean ± SD (Independent two-tailed t-test used to compare difference in CDC42, Rac1 and RhoA activity in monocytes plated on polyacrylamide hydrogels (0.15%) compared to floating control monocytes (N = 5)). G-LISA assay of small GTPases CDC42, Rac1 and RhoA in UB068 (black) and UB068_CHRFAM7A (orange) BGT treated (middle panel), and TG treated (bottom panel) isogenic monocytes. Data are presented as mean ± SD (Independent two-tailed t-test, change in CDC42, Rac1 and RhoA activity before and after drug treatment (N = 2)). f. Pharmacological modulation of preferred membrane structure in UB068 and UB068_CHRFAM7A isogenic monocytes by BGT and TG treatment. BGT treatment of UB068 and UB068_CHRFAM7A isogenic monocytes on 0.15% polyacrylamide hydrogels confirm α7 nAChR dependence by inhibition of the preferred membrane structure: inhibition of filopodia (III) and inhibition of lamellipodia (V). TG, a SERCA inhibitor that depletes ER Ca^{2+} reservoir and reduces amplitude of Ca^{2+} dynamics, switches filopodia (I) to lamellipodia (V) in UB068 monocytes. Scale bar, 20 µm.

derived monocytes (Fig. 3e (top panel) and Fig. 3f (I and II)).[55]

Using pharmacological modulation, we were able to switch membrane phenotypes: BGT treatment of null and CHRFAM7A (D) monocytes on 0.15% polyacrylamide hydrogels confirmed α 7 nAChR dependence by inhibition of the preferred membrane structure (Fig. 3f): inhibition of filopodia in null (Fig. 3f (I and III)) and inhibition of lamellipodia in CHRFAM7A monocytes (Fig. 3f (II and IV)). The inhibition of the membrane structure was accompanied by a decrease in CDC42 activation in null and a decrease in Rac1 activation in CHRFAM7A monocytes (Fig. 3e (middle panel)). TG shifted the preferred membrane structure towards lamellipodia in null cells (Fig. 3f (I and V)) which was accompanied by an increase in Rac1 activation (Fig. 3e (bottom panel)). TG did not affect the membrane structure in CHRFAM7A monocytes (Fig. 3f (II and VI). Of note in null monocytes, ER Ca^{2+} depletion mimics the effect of CHRFAM7A (Fig. 3f (I, II, and V)).

Taken together the electrophysiological, Ca^{2+} signalling, small GTPase activation and actin cytoskeleton rearrangement, we propose the following model: hypomorphic and partially ER retained α7/CHRFAM7A nAChR shifts the cytoplasmic Ca^{2+} signal source from the extracellular space to the ER reservoir and enhances ER leak. These changes lead to more autonomous Ca^{2+} dynamics and spontaneous Ca^{2+} oscillations. The change in amplitude and intracellular distribution of Ca^{2+} activates Rac1 leading to actin cytoskeleton reorganization in the form of lamellipodia.[57] Downstream actin effectors have been studied extensively in the innate immune system and have been linked to migration, cytokine transcriptional regulation and inflammasome activation.[58,59] Further work is needed to fully elucidate the downstream actin effectors and to characterize whether their regulation is through Rac1 or through other Ca^{2+} decoders.

Adaptation to tissue stiffness

Structural and mechanical adaptation of the cells is driven by the actin cytoskeleton.[60] As α7/CHRFAM7A nAChR initiates actin cytoskeleton changes, we explored cellular behaviour in more biologically relevant mechanical microenvironments using hydrogels.[61] Hydrogels mimic defined tissue stiffness, relevant to both physiological and pathological conditions.[61] We tested the morphological phenotype in a series of hydrogels spanning 2–30 kPa of elastic modulus, modelling the microenvironment from almost fluid state to fibrosis (Fig. 4a). Monocytes retained their preferred membrane structure (null - filopodia, CHRFAM7A - lamellipodia) all through the different hydrogel stiffnesses (Fig. 4b). The series of hydrogels revealed morphological adaptive response in the CHRFAM7A monocytes from low (0.03%) to high (0.6%) stiffness conditions, while null monocytes exhibited minimal adaptation (Fig. 4b and c). Maximum distance between curves (D) and significance of the analysed morphological parameters are depicted in Fig. 4d.

We used BGT and TG to elucidate the adaptive mechanism at low and high stiffness conditions. In the low stiffness environment (0.03% hydrogel), BGT had no effect (Fig. 4e) in either line. In contrast, TG inhibited the morphological adaptation in both null and CHRFAM7A monocytes, highlighting the role of the ER reservoir in maintaining the morphological adaptation (Fig. 4e). Of note, the Maximum distance between curves (D) of the adaptation that is blocked is higher in CHRFAM7A monocytes, suggesting an additional ER dependent mechanism, the previously discussed ER leak. In the high stiffness environment, BGT blocked morphological adaptation in CHRFAM7A monocytes with no effect on null cells (Fig. 4f), suggesting that morphological adaptation is α7/CHRFAM7A nAChR dependent gain of function (GOF) in stiff environment.

Atomic Force Microscopy (AFM) of single cells demonstrated adaptive intracellular stiffness response to hydrogel stiffness on fibronectin-coated low (0.03), intermediate (0.15), or high (0.6) stiffness hydrogels in CHRFAM7A monocytes, in contrast to null (Fig. 4g). The adaptive response, both morphological (Supplementary Fig. S3, and Supplementary Table S2) and intracellular stiffness occurred between 0.03% and 0.15% hydrogels corresponding to the shift between physiological and pathological conditions in humans (Fig. 4a, red bar).[62,63]

These cellular responses imply that CHRFAM7A enables cellular adaptation to the mechanical properties of the tissue environment through modulation of Ca^{2+} dynamics (soft)[64,65] and through PM localized α7/CHRFAM7A nAChR (stiff).[62,63] During evolution, tissue and organ specialization lead to diversity in tissue mechanics which is affected by pathological processes (Fig. 4a). Human monocyte mechanosensation modulated by α7/CHRFAM7A nAChR is a gain of function (GOF) that facilitates cellular adaptation to these changes.[66,67] We hypothesize that this cellular adaptation to the tissue environment represents innate immune GOF in immune surveillance, as the adaptive cells can reach tissues that otherwise have been immune restricted.

Cellular adhesion, motility, and phagocytosis

As actin cytoskeleton is central to adhesion, cellular motility and phagocytosis,[68] we proceeded to study these phenotypes in iPSC derived and primary human monocytes. The presence of CHRFAM7A in the isogenic monocytes resulted in distinct adhesion features and type of cellular motility. Null cells demonstrated focal distribution of the cellular adhesion proteins actin, vinculin and VASP (Fig. 5a). In CHRFAM7A cells, adhesion proteins colocalized into podosomes spaced along the lamellipodia (Fig. 5a).

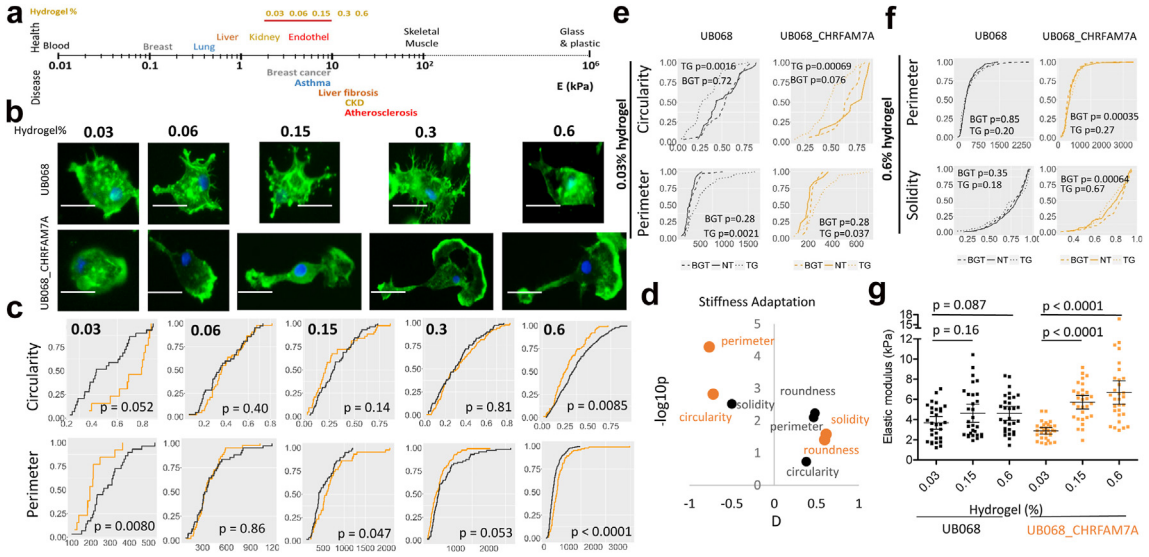

***Fig. 4:* Adaptation to tissue stiffness**. a. Schematic depicting tissue stiffness measured as elastic modulus in kPa modelled by various concentrations of polyacrylamide hydrogels indicated in gold. Tissue stiffness in examples of physiological (top) and pathological (bottom) conditions (based on data from animal models) are shown. b. EVOS FL fluorescent images (objective 20×) of phalloidin stained UB068 and UB068_CHRFAM7A isogenic monocytes on a series of fibronectin-coated hydrogels from 0.03 through 0.6 corresponding to a range of elastic modulus from 2 to 30 kPa. Genotype specific preferred membrane structure is sustained at each stiffness; CHRFAM7A monocytes demonstrate adaptive morphology over the stiffness gradient. Scale bar, 20 µm. c. Operator independent morphological analysis of UB068 (black) and UB068_CHRFAM7A (orange) isogenic monocytes plated on the hydrogel gradient. UB068_CHRFAM7A (orange graph) monocytes show circularity and perimeter adaptation in opposite direction from low to high stiffness while UB068 (black graph) shape is constant over the hydrogel gradient (black). Represented as cumulative density curves (Two-sample KS statistics, Bonferroni corrected p-values)). d. Morphological adaptation of UB068 (black) and UB068_CHRFAM7A (orange) isogenic monocytes between 0.03 and 0.15% polyacrylamide hydrogel are depicted in the volcano plot (Two-sample KS statistics, maximum distance between curves (D) versus -log(p)). e. Pharmacological modulation with BGT and TG on low (0.03) stiffness hydrogel indicates that low stiffness adaptation is TG (Ca^{2+}) dependent in both UB068 (black) and UB068_CHRFAM7A (orange) isogenic monocytes, albeit larger effect in UB068_CHRFAM7A (Two-sample KS statistics, Bonferroni corrected p-values)). f. On high (0.6) stiffness hydrogel, BGT blocks adaptation of UB068_CHRFAM7A (orange) monocytes indicating that high stiffness adaptation is BGT (α7/CHRFAM7A nAChR) dependent. One-dimensional cumulative distribution curves of morphological characteristics are depicted. (c, e, f: N = 3–7, 250–350 cells per genotype, Two-sample KS statistics, Bonferroni corrected p-values). g. Atomic Force microscopy (AFM). Cells were seeded on fibronectin-coated low (0.03%), intermediate (0.15%), or high (0.6%) stiffness hydrogels for 1 h. AFM was performed to measure intracellular stiffness. The stiffness data was summarized as scatter plot. (N = 3, 30 cells per condition, bars show mean ± 95% CI. Statistical tests were performed by independent two-tailed t-tests, Bonferroni corrected p-values.).

These distinct adhesion patterns resulted in differences in adhesion properties of the cells to various matrices (Fig. 5b). Null cells demonstrated higher adhesion to laminin compared to CHRFAM7A monocytes consistent with the focal adhesion detected by the ICC. Focal adhesions are mediated by laminin-integrin interaction.[69,70] In contrast, CHRFAM7A monocytes had higher adhesion to Geltrex, which in addition to laminin, contains collagen IV, entactin, and heparan sulphate proteoglycans and is considered as a model of the basement membrane.[71]

Cellular motility of null and CHRFAM7A monocytes are defined by their actin cytoskeleton and adhesion phenotypes. When exposed to chemoattractant CXCL12, null monocytes migrated through transwell inserts (Fig. 5c). In contrast, in the experimental system when transwells are coated with Matrigel, CHRFAM7A monocytes were able to invade and transgress the coated inserts while null monocytes were unable to respond to the chemoattractant (Fig. 5d). In human primary monocytes *CHRFAM7A* noncarriers exhibited higher migration ability while carriers favoured invasion as cellular locomotion (Fig. 5e and f). Pharmacological modulation with small GTPase inhibitors showed that migration in response to CXCL12 is RhoA dependent in null monocytes (reduced by RhoA antagonist Rhosin) (Fig. 5g). In CHRFAM7A monocytes, invasion was blocked by Rac1 inhibitor EHT1864 (Fig. 5h), validating the proposed mechanism of CHRFAM7A associated Rac1 activation.[29]

Morphologically CHRFAM7A monocytes achieved the invasion GOF with the lamellipodia structure (Fig. 5a, lower panel) and podosome distribution along the lamellipodia (Fig. 5a, lower panel).[72] Fluorescent collagen degradation images (Fig. 5i) demonstrated that null monocytes have an accumulation of collagen

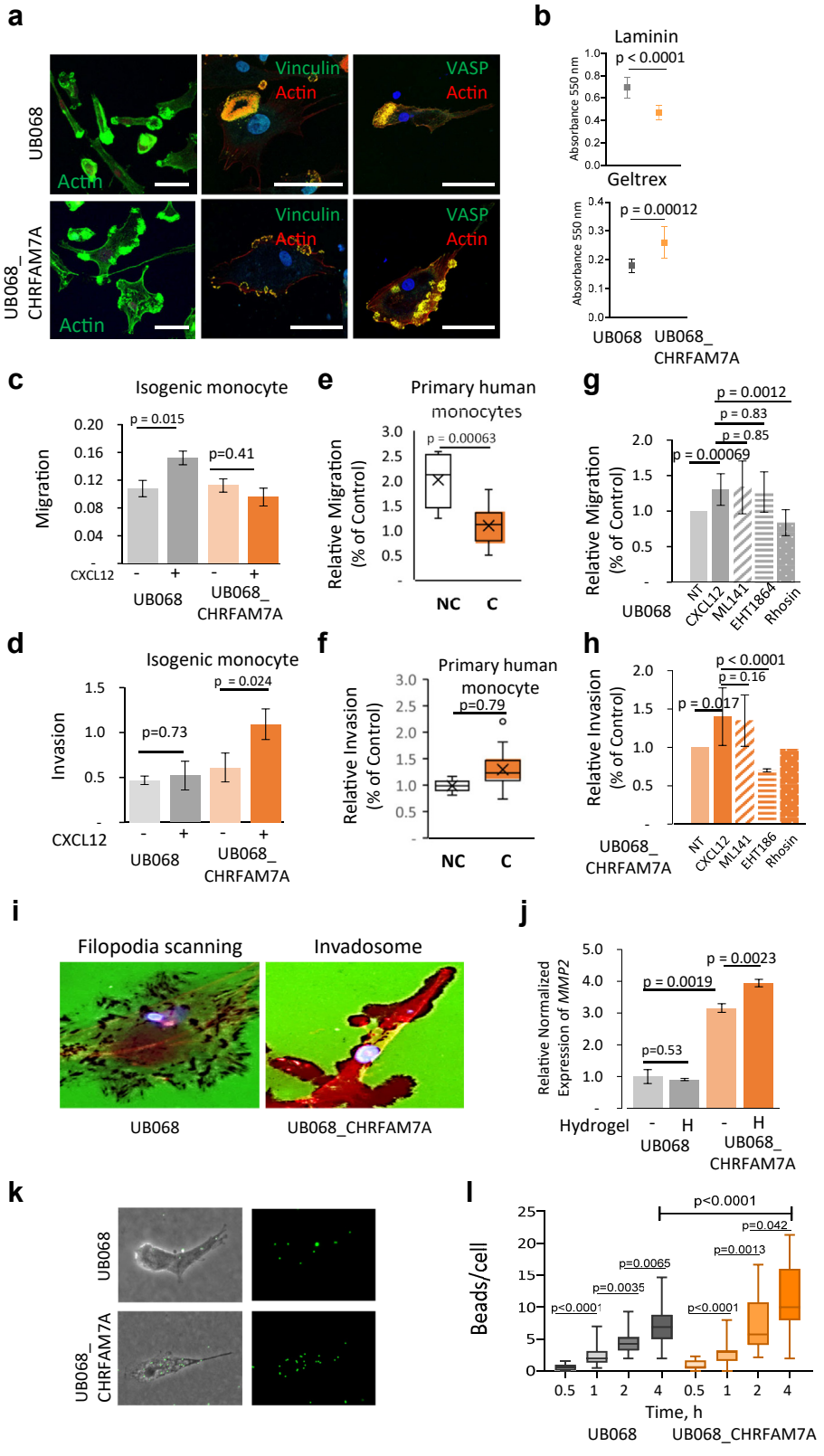
a
UB068
UB068_ CHRFAM7A
Actin
Vinculin
VASP
b
Laminin
p < 0.0001
Absorbance 550 nm
Geltrex
p = 0.00012
UB068
UB068_ CHRFAM7A
c
Isogenic monocyte
Migration
p = 0.015
p=0.41
CXCL12
UB068
UB068_ CHRFAM7A
e
Primary human monocytes
Relative Migration (% of Control)
p = 0.00063
NC
C
g
Relative Migration (% of Control)
p = 0.0012
p = 0.83
p = 0.85
p = 0.00069
NT
CXCL12
ML141
EHT1864
Rhosin
d
Isogenic monocyte
Invasion
p = 0.024
p=0.73
f
Primary human monocyte
Relative Invasion (% of Control)
p=0.79
h
Relative Invasion (% of Control)
p < 0.0001
p = 0.16
p = 0.017
EHT186
i
Filopodia scanning
Invadosome
UB068
UB068_CHRFAM7A
j
Relative Normalized Expression of MMP2
p = 0.0023
p = 0.0019
p=0.53
Hydrogel
k
l
Beads/cell
p<0.0001
p=0.042
p=0.0013
p=0.0065
p=0.0035
Time, h

degradation puncta (Fig. 5i, left panel) consistent with filopodia exploratory movement.[73] In contrast, CHRFAM7A monocytes have podosomes spaced along the lamellipodia (Fig. 5i, right panel) that create a collagen degradation pattern that follows the lamellipodia outline.[74] The invasion GOF is congruent with increased *MMP2* expression in CHRFAM7A monocytes at baseline and when exposed to hydrogels (Fig. 5j).

Both in the iPSC model and in primary monocytes, non-carriers of CHRFAM7A demonstrated filopodia and focal adhesion consistent with migration, while CHRFAM7A carriers showed lamellipodia, podosomal-type adhesion, and increased *MMP2* expression leading to invasion GOF consistent with current understanding of the mechanism of cellular locomotion.[75–77]

Phagocytosis is an essential component of tissue homeostasis and the innate immune response.[78] The process requires profound reorganization of the cell morphology around the target in a controlled manner. Critical aspects of the interaction between receptors, membrane, and the actin cytoskeleton have been identified.[79] To evaluate the effect of CHRFAM7A mediated actin cytoskeleton GOF we performed time course experiments of 1 μm FluoroSpheres uptake as a phagocytosis assay. Both cell lines demonstrated time dependent uptake of the beads. CHRFAM7A isogenic monocytes demonstrated more efficient phagocytosis all through the time course, reaching statistical significance at 4 h (Fig. 5k and l).

In summary, all three actin cytoskeleton phenotypes, cellular adhesion, motility and phagocytosis reveal a CHRFAM7A mediated innate immune gain of function. This gain of function is due to actin cytoskeleton reorganization through Rac1 by resetting Ca^{2+} signalling.

Discussion

CHRFAM7A, a human restricted fusion gene between *CHRNA7* and *ULK4*[2] is a negative regulator of the α7 nAChR.[17–20,24] Human restricted genes are of importance as they can contribute to human specific traits and to the translational gap in drug development.[17] Large scale functional annotation of human restricted genes revealed their role in immune adaptation, development of the human brain and adaptation involving metabolic processes[1] aligning with the innate immune GOF presented here. Mechanistically, human specific fusion genes frequently act as a negative regulator of a canonical pathway resulting in a biological gain of function with selective advantage. *SRGAP2* has two human-specific duplication alleles, *SRGAP2B* and *SRGAP2C*. The duplications are partial and encode a truncated F-BAR domain. SRGAP2C dimerizes with ancestral SRGAP2 to inhibit its function, releases the block of radial migration, resulting in the evolution of the human neocortex.[80,81] *ARHGAP11B*, another human restricted partial duplication, promotes basal progenitor generation, increasing cortical plate area and inducing gyrification.[82] We have previously shown that the hypomorphic α7/CHRFAM7A nAChR releases NFκB inhibition in microglia, switching from anti-inflammatory to proinflammatory state.[19] In the context of immune surveillance, α7/CHRFAM7A nAChR mitigates the control of Ca^{2+} dynamics by the extracellular space

***Fig. 5:* Cellular adhesion, motility, and phagocytosis**. a. Representative confocal images demonstrating differences in focal adhesion between UB068 and UB068_CHRFAM7A derived macrophages. Note the monolateral distribution of the cellular adhesion proteins in the null macrophages versus bilateral – in the direct. Podosomes are visualized by actin/vinculin or actin/VASP staining. Scale bar, 50 μm. b. Quantification of cell adhesion in the isogenic monocytes plated on laminin (upper panel) and Geltrex (lower panel). Spectrophotometric quantification of crystal violet stained cells represented as mean ± SD (N = 3, independent two-tailed t-tests, Bonferroni corrected p-values). c. Migration assay on UB068 and UB068_CHRFAM7A isogenic monocytes plated on transwell inserts with and without chemoattractant CXCL12 in lower chamber for 16 h. Spectrophotometric quantification of crystal violet stained cells in lower chamber are depicted as mean ± SD (N = 3, independent two-tailed t-test). d. Invasion assay on UB068 and UB068_CHRFAM7A isogenic monocytes plated on 8 mg/ml Matrigel coated transwell inserts with and without chemoattractant CXCL12 for 16 h. Spectrophotometric quantification of crystal blue stained cells in lower chamber (N = 3–5, depicted mean ± SD, independent two-tailed t-test). e. Migration through transwell inserts of primary human monocytes from 12 donors in 24 independent experiments. Box plots depict relative absorption of crystal violet stained cells in lower chamber in Noncarrier (black) and Carrier (orange) primary human monocytes (independent two-tailed t-test). f. Matrigel coated transwell invasion assay of primary human monocytes from 9 donors in 18 independent experiments (Box plots depict relative absorption of crystal violet stained cells in lower chamber). g. Pharmacological modulation of migration of UB068 isogenic monocytes with small GTPase inhibitors. Monocytes were plated with or without CDC42 (ML 141), RhoA (Rhosin) and Rac1(EHT 1862) inhibitors. Spectrophotometric quantification of crystal violet stained cells in lower chamber. (N = 3–5, depicted as mean ± SD, independent two-tailed t-test). h. Pharmacological modulation of invasion with small GTPase inhibitors in UB068_CHRFAM7A isogenic monocytes. Monocytes were plated on Matrigel coated transwell inserts with or without CDC42 (ML141), RhoA (Rhosin) and Rac1 (EHT 1862) inhibitors. (N = 3–5, depicted as mean ± SD, independent two-tailed t-test). i. Representative images of UB068 and UB068_CHRFAM7A isogenic monocytes plated on fluorescent collagen for 16 h. Black pixels depict degradation. j. *MMP2* gene expression levels of UB068 and UB068_CHRFAM7A monocytes at baseline and upon exposure to fibronectin coated hydrogel for 1 h (N = 3–5, depicted as mean ± SD, independent two-tailed t-test). k. Representative images of UB068 and UB068_CHRFAM7A isogenic macrophages incubated for 4 h with 1 μm polystyrene yellow green FluoSpheres. l. Quantification of time-dependent phagocytosis of 1 μm polystyrene yellow green FluoSpheres in UB068 and UB068_CHRFAM7A isogenic macrophages depicted as Box plots (N = 3, 30–50 cells/condition per experiment; Mann–Whitney U-test with Bonferroni multiple testing correction).

creating cell autonomous Ca^{2+} oscillations leading to actin cytoskeleton GOF.

CHRFAM7A is the result of complex chromosomal rearrangements, including duplication, deletion and inversion events on chromosome 15 during evolution.[2] As it is not present in any other species, the function of CHRFAM7A remains unexplored. Recently, two studies reported on CHRFAM7A function in transgenic mouse models, suggesting a role in inflammation and neurodegeneration,[83,84] aligning with the large scale annotation.[1] The immune phenotype of the CHRFAM7A KI mice revealed a shift towards the monocytic lineage and increased monocytic presence in the damaged lung tissue which was protective from secondary infection in a burn model.[83]

While electrophysiological studies have shown that incorporation of CHRFAM7A into the α7 nAChR pentamer results in decreased channel open probability leading to a hypomorphic receptor,[17,18,49] the effect on Ca^{2+} signalling was in need of further characterization.[28,29] We systematically assessed the effect of CHRFAM7A on Ca^{2+} oscillations using live cell Fluo-4 imaging. Using modelling and Bayesian inference the Ca^{2+} signal changes are identified as a shift in utilization of Ca^{2+} from extracellular space (hypomorphic α7/CHRFAM7A nAChR) to intracellular (ER) reservoir. Furthermore, the increased ER leak leads to resetting the Ca^{2+} steady state in the cytoplasm and cell autonomous spontaneous oscillations.[85] Pharmacological responses depicted a unique difference in the cytoplasmic Ca^{2+} signal: paradoxical increase in amplitude upon BGT treatment in both the isogenic model and human primary monocytes aligning with the hypothesis that intracellular processes are driving the Ca^{2+} dynamics in the presence of CHRFAM7A. Paradoxical increase upon treatment with ER reservoir sparing agents (U73122 and Xesto) further support the ER leak mechanism due to the retention of the α7/CHRFAM7A nAChR in the ER, likely due to decreased glycosylation of the fusion protein.[54,86]

These data provide mechanistic insights to some of the biological outcomes reported in the CHRFAM7A mouse burn model.[83] Lung burn injury implicates a diseased lung tissue with increased stiffness of the ECM.[64] CHRFAM7A KI mice were able to fend off secondary bacterial infection due to a second wave of macrophages populating the diseased lung tissue.[83] Actin has been designated as mechanically adaptive material.[60] We show that the reset of Ca^{2+} signalling activates Rac1 and infers actin cytoskeleton reorganization.[87] The functional outcome is a cell that adapts to the mechanical properties of the tissue and switches to invasion as a cellular motility strategy.[88] Podosome distribution and *MMP2* gene expression support the invasion GOF.[89] The increased adaptation to the mechanical properties of the tissue and invasion as the cellular motility form align with the biological observations in the CHRFAM7A KI burn model.[83] Of note, the hypothesis that cellular motility is affected by CHRFAM7A was tested in an *in vitro* migration assay, which showed decreased migration of CHRFAM7A monocytes[60] similar to our isogenic iPSC derived monocytes; however, invasion was not assessed in that study.

There are several limitations to our study that invite caution and further work. The experiments are cell based *in vitro* observations albeit resulted in congruent results between iPSC derived isogenic monocytes and human primary monocytes from 30 donors. These similar observations suggest that the phenotypes in the iPSC model are not related to overexpression of CHRFAM7A. We highlight the mechanism of Ca^{2+} dynamics and its biological outcomes through small GTPase Rac1. Lamellipodia formation is linked to actin branching driven by Wave and (Arp)2/3 complex.[57] To fully characterize the signalling pathways affected by CHRFAM7A, additional experiments may be needed. Small GTPases have been implicated in migration, inflammasome activation and transcriptional regulation of cytokines,[58,59] for example regulation of NADPH and NFκB. Downstream of Rac1 a whole array of actin effectors has been characterized[58,59] which needs a complex set of experiments. Ca^{2+} signalling being the central mechanism upstream of Rac1 opens a whole new area of inquiry on Rac1 independent Ca^{2+} decoding, for example how CHRFAM7A may affect the combinatorial transcriptional regulation in the innate immune system as all master transcription factors are Ca^{2+} decoders, including NFAT, NFκB and AP1.[90,91]

We also note the potential for confounding factors in the presented between-group comparisons, and thus additional, larger studies will be required in order to statistically adjust for subject specific variables related to outcome.

The function of the inverted allele remains elusive. There is compelling evidence that the inverted allele is null from the perspective of the α7 nAChR[17] and predicted to be non-translated.[2] However, allele frequency in the human population is similar to the direct allele indicating strong selective pressure for the inverted allele as well.[17] The genetic mechanism and functional consequences of the inverted allele needs further work to screen for α7 nAChR independent mechanisms.

The isogenic iPSC model enabled us to define allele specific gain of function in contrast to null, shedding light on evolutionary aspects and suggesting immune spatial vigilance as a selective pressure for enrichment of *CHRFAM7A* in the human population. Importantly, CHRFAM7A is not only human specific, it also has diversity as 25% of humans are noncarriers of the functional allele while 75% are carriers.[17] This 1:3 split predicts profound translational significance. Although much work is needed, these observations open new opportunities to explore human biology in the context of

this binomial diversity. It is plausible that clinical outcomes of drugs affecting this pathway would be different in carriers versus noncarriers of the hypomorphic α7/CHRFAM7A nAChR, depending upon the disease and the mechanism involved.[17] CHRFAM7A has been implicated in systemic inflammatory response,[92] inflammatory bowel disease,[93] COVID associated cytokine storm,[94] HIV-associated neurocognitive disorders,[95] osteoarthritis,[96] and cancer metastasis.[64,97] Utilizing *CHRFAM7A* genotype in pharmacogenetic clinical trial design can lead to successful drug development. As Ca^{2+} signalling drives fundamental biological processes overarching cellular metabolism, migration, invasion, proliferation and apoptosis, other biological and pathological processes are likely affected by CHRFAM7A.

Contributors

K.S. conceptualized and designed the study, both the laboratory experiments and clinical aspects, led the wet lab and human experimental design, data analysis and data interpretation, and wrote the first draft of the manuscript. I.I. performed the iPSC and primary human culture experiments, contributed to data analysis and interpretation, and worked extensively on the manuscript. Em.N. performed iPSC and primary human culture experiments and contributed to data analysis, statistical analysis, and figures. R.P.D. contributed to G-LISA and calcium experiments, performed statistical analysis, and contributed to data analysis and figures. I.M. conducted calcium imaging on iPSC-derived and primary human monocytes and performed the Min1Pipe and CaBBI analyses. M.H. contributed to calcium data analysis and this section figures. B.B. contributed to the genome editing of the iPSC line. S.P. performed the morphological analyses in ImageJ and statistics. R.S.B. contributed to adhesion and phagocytosis experiments. D.C.I. performed the patch clamp experiments and contributed the electrophysiological sections of the manuscript. Er.N. performed AFM experiments and data analysis. Y.H. contributed to the mechanosensation experiments. K.R. performed calcium data analysis and statistics in MathLab. L.C. performed data capture and analysis of the flow cytometry experiment. N.S. contributed to study conceptualization and design, supervised monocyte characterization, and critically reviewed the manuscript. W.A.H. contributed to the design of calcium imaging experiments and analysis. A.A. designed the electrophysiological experiments and contributed to those sections of the manuscript. G.W. supervised statistical analysis of the data and critically read the manuscript. Y.B. designed the AFM experiments, contributed to data interpretation for mechanosensation and actin cytoskeleton mechanism and critically read the manuscript. J.R. co-designed the human experiments, submitted the IRB and supervised the primary human monocyte isolation and characterization, contributed to data interpretation from the immunology perspective, and critically read the manuscript.

K.S., Y.B., and J.R. had accessed and verified the underlying data.

All authors read and approved the final version of the manuscript.

Data sharing statement

The data that support the findings of this study are available from the corresponding author (K.S.), upon reasonable request.

Declaration of interests

The authors declare no competing interests.

Acknowledgements

We thank contributors who collected samples used in this study, as well as human donors, whose help and participation made this work possible.

This work is supported in part by the Community Foundation for Greater Buffalo (Kinga Szigeti) and in part by NIH grant R01HL163168 (Yongho Bae).

Appendix A. Supplementary data

Supplementary data related to this article can be found at https://doi.org/10.1016/j.ebiom.2024.105093.

References

1 Bitar M, Kuiper S, O'Brien EA, Barry G. Genes with human-specific features are primarily involved with brain, immune and metabolic evolution. *BMC Bioinformatics*. 2019;20(Suppl 9):406.
2 Sinkus ML, Graw S, Freedman R, Ross RG, Lester HA, Leonard S. The human CHRNA7 and CHRFAM7A genes: a review of the genetics, regulation, and function. *Neuropharmacology*. 2015;96(Pt B):274–288.
3 Borroni V, Barrantes FJ. Homomeric and heteromeric α7 nicotinic acetylcholine receptors in health and some central nervous system diseases. *Membranes*. 2021;11(9):664.
4 Broide RS, Winzer-Serhan UH, Chen Y, Leslie FM. Distribution of α7 nicotinic acetylcholine receptor subunit mRNA in the developing mouse. *Front Neuroanat*. 2019;13.
5 Kalkman HO, Feuerbach D. Modulatory effects of alpha 7 nAChRs on the immune system and its relevance for CNS disorders. *Cell Mol Life Sci*. 2016;73(13):2511–2530.
6 Mizrachi T, Vaknin-Dembinsky A, Brenner T, Treinin M. Neuroinflammation modulation via α7 nicotinic acetylcholine receptor and its chaperone, RIC-3. *Molecules*. 2021;26(20):6139.
7 de Jonge WJ, Ulloa L. The alpha 7 nicotinic acetylcholine receptor as a pharmacological target for inflammation. *Br J Pharmacol*. 2007;151(7):915–929.
8 Wang H, Yu M, Ochani M, et al. Nicotinic acetylcholine receptor alpha 7 subunit is an essential regulator of inflammation. *Nature*. 2003;421(6921):384–388.
9 Wu YJ, Wang L, Ji CF, Gu SF, Yin Q, Zuo J. The role of alpha7nAChR-mediated cholinergic anti-inflammatory pathway in immune cells. *Inflammation*. 2021;44(3):821–834.
10 Costantini TW, Dang X, Coimbra R, Eliceiri BP, Baird A. CHRFAM7A, a human-specific and partially duplicated alpha 7-nicotinic acetylcholine receptor gene with the potential to specify a human-specific inflammatory response to injury. *J Leukoc Biol*. 2015;97(2):247–257.
11 Villiger Y, Szanto I, Jaconi S, et al. Expression of an alpha 7 duplicate nicotinic acetylcholine receptor-related protein in human leukocytes. *J Neuroimmunol*. 2002;126(1-2):86–98.
12 Benfante R, Antonini RA, De Pizzol M, et al. Expression of the alpha 7 nAChR subunit duplicate form (CHRFAM7A) is down-regulated in the monocytic cell line THP-1 on treatment with LPS. *J Neuroimmunol*. 2011;230(1-2):74–84.
13 Maroli A, Di Lascio S, Drufuca L, et al. Effect of donepezil on the expression and responsiveness to LPS of CHRNA7 and CHRFAM7A in macrophages: a possible link to the cholinergic anti-inflammatory pathway. *J Neuroimmunol*. 2019;332:155–166.
14 Di Lascio S, Fornasari D, Benfante R. The human-restricted isoform of the alpha 7 nAChR, CHRFAM7A: a double-edged sword in neurological and inflammatory disorders. *Int J Mol Sci*. 2022;23(7):3463.
15 Peng W, Mao L, Dang X. The emergence of the uniquely human α7 nicotinic acetylcholine receptor gene and its roles in inflammation. *Gene*. 2022;842:146777.
16 Maldifassi MC, Martin-Sanchez C, Atienza G, et al. Interaction of the alpha 7-nicotinic subunit with its human-specific duplicated dupalpha7 isoform in mammalian cells: relevance in human inflammatory responses. *J Biol Chem*. 2018;293(36):13874–13888.
17 Szigeti K, Ihnatovych I, Birkaya B, et al. CHRFAM7A: a human specific fusion gene, accounts for the translational gap for cholinergic strategies in Alzheimer's disease. *eBioMedicine*. 2020;59:102892.
18 Ihnatovych I, Nayak TK, Ouf A, et al. iPSC model of CHRFAM7A effect on alpha 7 nicotinic acetylcholine receptor function in the human context. *Transl Psychiatry*. 2019;9(1):59.
19 Ihnatovych I, Birkaya B, Notari E, Szigeti K. iPSC-derived microglia for modeling human-specific DAMP and PAMP responses in the context of alzheimer's disease. *Int J Mol Sci*. 2020;21(24):9668.
20 de Lucas-Cerrillo AM, Maldifassi MC, Arnalich F, et al. Function of partially duplicated human alpha77 nicotinic receptor subunit CHRFAM7A gene: potential implications for the cholinergic anti-inflammatory response. *J Biol Chem*. 2011;286(1):594–606.
21 Wang Y, Xiao C, Indersmitten T, Freedman R, Leonard S, Lester HA. The duplicated alpha7 subunits assemble and form

functional nicotinic receptors with the full-length alpha7. *J Biol Chem*. 2014;289(38):26451–26463.
22 Lasala M, Corradi J, Bruzzone A, Esandi MDC, Bouzat C. A human-specific, truncated alpha7 nicotinic receptor subunit assembles with full-length alpha7 and forms functional receptors with different stoichiometries. *J Biol Chem*. 2018;293(27):10707–10717.
23 Ihnatovych I, Lew A, Lazar E, Sheng A, Kellermayer T, Szigeti K. Timing of Wnt inhibition modulates directed differentiation of medial ganglionic eminence progenitors from human pluripotent stem cells. *Stem Cells Int*. 2018;2018:3983090.
24 Araud T, Graw S, Berger R, et al. The chimeric gene CHRFAM7A, a partial duplication of the CHRNA7 gene, is a dominant negative regulator of alpha7*nAChR function. *Biochem Pharmacol*. 2011;82(8):904–914.
25 Shen JX, Yakel JL. Nicotinic acetylcholine receptor-mediated calcium signaling in the nervous system. *Acta Pharmacol Sin*. 2009;30(6):673–680.
26 King JR, Nordman JC, Bridges SP, Lin MK, Kabbani N. Identification and characterization of a G protein-binding cluster in alpha7 nicotinic acetylcholine receptors. *J Biol Chem*. 2015;290(33):20060–20070.
27 King JR, Ullah A, Bak E, Jafri MS, Kabbani N. Ionotropic and metabotropic mechanisms of allosteric modulation of alpha7 nicotinic receptor intracellular calcium. *Mol Pharmacol*. 2018;93(6):601–611.
28 Martín-Sánchez C, Alés E, Balseiro-Gómez S, et al. The human-specific duplicated α7 gene inhibits the ancestral α7, negatively regulating nicotinic acetylcholine receptor-mediated transmitter release. *J Biol Chem*. 2021;296:100341.
29 Szigeti K, Ihnatovych I, Rosas N, et al. Neuronal actin cytoskeleton gain of function in the human brain. *eBioMedicine*. 2023;95:104725.
30 van Wilgenburg B, Browne C, Vowles J, Cowley SA. Efficient, long term production of monocyte-derived macrophages from human pluripotent stem cells under partly-defined and fully-defined conditions. *PLoS One*. 2013;8(8):e71098.
31 Lu J, Li C, Singh-Alvarado J, et al. MIN1PIPE: a miniscope 1-Photon-based calcium imaging signal extraction pipeline. *Cell Rep*. 2018;23(12):3673–3684.
32 Rahmati V, Kirmse K, Markovic D, Holthoff K, Kiebel SJ. Inferring neuronal dynamics from calcium imaging data using biophysical models and bayesian inference. *PLoS Comput Biol*. 2016;12(2):e1004736.
33 Daunizeau J, Adam V, Rigoux L. VBA: a probabilistic treatment of nonlinear models for neurobiological and behavioural data. *PLoS Comput Biol*. 2014;10(1):e1003441.
34 Li YX, Rinzel J. Equations for InsP3 receptor-mediated [Ca2+]i oscillations derived from a detailed kinetic model: a Hodgkin-Huxley like formalism. *J Theor Biol*. 1994;166(4):461–473.
35 Nadkarni S, Jung P. Modeling synaptic transmission of the tripartite synapse. *Phys Biol*. 2007;4(1):1–9.
36 Han JM, Tanimura A, Kirk V, Sneyd J. A mathematical model of calcium dynamics in HSY cells. *PLoS Comput Biol*. 2017;13(2):e1005275.
37 Yao J, Pilko A, Wollman R. Distinct cellular states determine calcium signaling response. *Mol Syst Biol*. 2016;12(12):894.
38 Klein EA, Yung Y, Castagnino P, Kothapalli D, Assoian RK. Cell adhesion, cellular tension, and cell cycle control. *Methods Enzymol*. 2007;426:155–175.
39 Brazzo JA, Biber JC, Nimmer E, et al. Mechanosensitive expression of lamellipodin promotes intracellular stiffness, cyclin expression and cell proliferation. *J Cell Sci*. 2021;134(12):jcs257709.
40 Aumailley M. Chapter 11 - isolation and analysis of laminins. In: Mecham RP, ed. *Methods in cell biology*. 143. Academic Press; 2018:187–205.
41 Enomoto R, Imamori M, Seon A, et al. Proposal for a new evaluation of phagocytosis using different sizes of fluorescent polystyrene microspheres. *Adv Biol Chem*. 2013;3:556–563.
42 Diaz B. Invadopodia detection and gelatin degradation assay. *Bio Protoc*. 2013;3(24):e997.
43 Nielsen MC, Andersen MN, Moller HJ. Monocyte isolation techniques significantly impact the phenotype of both isolated monocytes and derived macrophages in vitro. *Immunology*. 2020;159(1):63–74.
44 Chan T, Williams E, Cohen O, Eliceiri BP, Baird A, Costantini TW. CHRFAM7A alters binding to the neuronal alpha-7 nicotinic acetylcholine receptor. *Neurosci Lett*. 2019;690:126–131.
45 Liu D, de Souza JV, Ahmad A, Bronowska AK. Structure, dynamics, and ligand recognition of human-specific CHRFAM7A (Dupalpha7) nicotinic receptor linked to neuropsychiatric disorders. *Int J Mol Sci*. 2021;22(11):5466.
46 Skok MV. Editorial: to channel or not to channel? Functioning of nicotinic acetylcholine receptors in leukocytes. *J Leukoc Biol*. 2009;86(1):1–3.
47 Nurkhametova D, Siniavin A, Streltsova M, et al. Does cholinergic stimulation affect the P2X7 receptor-mediated dye uptake in mast cells and macrophages? *Front Cell Neurosci*. 2020;14:548376.
48 Siniavin AE, Streltsova MA, Kudryavtsev DS, Shelukhina IV, Utkin YN, Tsetlin VI. Activation of α7 nicotinic acetylcholine receptor upregulates HLA-DR and macrophage receptors: potential role in adaptive immunity and in preventing immunosuppression. *Biomolecules*. 2020;10(4):507.
49 Kabbani N, Nichols RA. Beyond the channel: metabotropic signaling by nicotinic receptors. *Trends Pharmacol Sci*. 2018;39(4):354–366.
50 Macmillan D, McCarron JG. The phospholipase C inhibitor U-73122 inhibits Ca(2+) release from the intracellular sarcoplasmic reticulum Ca(2+) store by inhibiting Ca(2+) pumps in smooth muscle. *Br J Pharmacol*. 2010;160(6):1295–1301.
51 Bill CA, Vines CM. Phospholipase C. *Adv Exp Med Biol*. 2020;1131:215–242.
52 Hollywood MA, Sergeant GP, Thornbury KD, McHale NG. The PI-PLC inhibitor U-73122 is a potent inhibitor of the SERCA pump in smooth muscle. *Br J Pharmacol*. 2010;160(6):1293–1294.
53 De Smet P, Parys JB, Callewaert G, et al. Xestospongin C is an equally potent inhibitor of the inositol 1,4,5-trisphosphate receptor and the endoplasmic-reticulum Ca(2+) pumps. *Cell Calcium*. 1999;26(1-2):9–13.
54 Kweon HJ, Gu S, Witham E, et al. NACHO engages N-glycosylation ER chaperone pathways for alpha7 nicotinic receptor assembly. *Cell Rep*. 2020;32(6):108025.
55 Ridley AJ. Life at the leading edge. *Cell*. 2011;145(7):1012–1022.
56 Schindelin J, Arganda-Carreras I, Frise E, et al. Fiji: an open-source platform for biological-image analysis. *Nat Methods*. 2012;9(7):676–682.
57 Krause M, Gautreau A. Steering cell migration: lamellipodium dynamics and the regulation of directional persistence. *Nat Rev Mol Cell Biol*. 2014;15(9):577–590.
58 Bokoch GM. Regulation of innate immunity by Rho GTPases. *Trends Cell Biol*. 2005;15(3):163–171.
59 Dipankar P, Kumar P, Dash SP, Sarangi PP. Functional and therapeutic relevance of Rho GTPases in innate immune cell migration and function during inflammation: an in silico perspective. *Mediators Inflamm*. 2021;2021:6655412.
60 Banerjee S, Gardel ML, Schwarz US. The actin cytoskeleton as an active adaptive material. *Annu Rev Condens Matter Phys*. 2020;11(1):421–439.
61 Luo T, Tan B, Zhu L, Wang Y, Liao J. A review on the design of hydrogels with different stiffness and their effects on tissue repair. *Front Bioeng Biotechnol*. 2022;10:817391.
62 Al-Sheikh U, Kang L. Mechanosensation: alpha-7 nAChR transduces sound signals in earless C. elegans. *Neuron*. 2021;109(22):3539–3541.
63 Iliff AJ, Wang C, Ronan EA, et al. The nematode C. elegans senses airborne sound. *Neuron*. 2021;109(22):3633–36346.e7.
64 Fang X, Ni K, Guo J, et al. FRET visualization of cyclic stretch-activated ERK via calcium channels mechanosensation while not integrin beta1 in airway smooth muscle cells. *Front Cell Dev Biol*. 2022;10:847852.
65 Miroshnikova YA, Manet S, Li X, Wickstrom SA, Faurobert E, Albiges-Rizo C. Calcium signaling mediates a biphasic mechanoadaptive response of endothelial cells to cyclic mechanical stretch. *Mol Biol Cell*. 2021;32(18):1724–1736.
66 Bird L. Monocytes feel the pressure. *Nat Rev Immunol*. 2019;19(10):595.
67 Solis AG, Bielecki P, Steach HR, et al. Mechanosensation of cyclical force by PIEZO1 is essential for innate immunity. *Nature*. 2019;573(7772):69–74.
68 Rodriguez OC, Schaefer AW, Mandato CA, Forscher P, Bement WM, Waterman-Storer CM. Conserved microtubule-actin interactions in cell movement and morphogenesis. *Nat Cell Biol*. 2003;5(7):599–609.
69 Geiger B, Boujemaa-Paterski R, Winograd-Katz SE, Balan Venghateri J, Chung WL, Medalia O. The actin network interfacing diverse integrin-mediated adhesions. *Biomolecules*. 2023;13(2):294.

70 Yamada M, Sekiguchi K. Molecular basis of laminin-integrin interactions. *Curr Top Membr*. 2015;76:197–229.
71 Baschieri F, Uetz-von Allmen E, Legler DF, Farhan H. Loss of GM130 in breast cancer cells and its effects on cell migration, invasion and polarity. *Cell Cycle*. 2015;14(8):1139–1147.
72 Chen YW, Lai CS, Chen YF, Chiu WT, Chen HC, Shen MR. STIM1-dependent Ca(2+) signaling regulates podosome formation to facilitate cancer cell invasion. *Sci Rep*. 2017;7(1):11523.
73 Kim MC, Silberberg YR, Abeyaratne R, Kamm RD, Asada HH. Computational modeling of three-dimensional ECM-rigidity sensing to guide directed cell migration. *Proc Natl Acad Sci U S A*. 2018;115(3):E390–E399.
74 Cambi A, Chavrier P. Tissue remodeling by invadosomes. *Fac Rev*. 2021;10:39.
75 Newby AC. Metalloproteinase expression in monocytes and macrophages and its relationship to atherosclerotic plaque instability. *Arterioscler Thromb Vasc Biol*. 2008;28(12):2108–2114.
76 Yu CF, Chen FH, Lu MH, Hong JH, Chiang CS. Dual roles of tumour cells-derived matrix metalloproteinase 2 on brain tumour growth and invasion. *Br J Cancer*. 2017;117(12):1828–1836.
77 Ma N, Xu E, Luo Q, Song G. Rac 1: a regulator of cell migration and a potential target for cancer therapy. *Molecules*. 2023;28(7):2976.
78 Lim JJ, Grinstein S, Roth Z. Diversity and versatility of phagocytosis: roles in innate immunity, tissue remodeling, and homeostasis. *Front Cell Infect Microbiol*. 2017;7:191.
79 Jaumouillé V, Waterman CM. Physical constraints and forces involved in phagocytosis. *Front Immunol*. 2020;11:1097.
80 Dennis MY, Nuttle X, Sudmant PH, et al. Evolution of human-specific neural SRGAP2 genes by incomplete segmental duplication. *Cell*. 2012;149(4):912–922.
81 Schmidt ERE, Kupferman JV, Stackmann M, Polleux F. The human-specific paralogs SRGAP2B and SRGAP2C differentially modulate SRGAP2A-dependent synaptic development. *Sci Rep*. 2019;9(1):18692.
82 Florio M, Albert M, Taverna E, et al. Human-specific gene ARHGAP11B promotes basal progenitor amplification and neocortex expansion. *Science*. 2015;347(6229):1465–1470.
83 Costantini TW, Chan TW, Cohen O, et al. Uniquely human CHRFAM7A gene increases the hematopoietic stem cell reservoir in mice and amplifies their inflammatory response. *Proc Natl Acad Sci U S A*. 2019;116(16):7932–7940.
84 Jiang Y, Yuan H, Huang L, Hou X, Zhou R, Dang X. Global proteomic profiling of the uniquely human CHRFAM7A gene in transgenic mouse brain. *Gene*. 2019;714:143996.
85 Schulte A, Blum R. Shaped by leaky ER: homeostatic Ca(2+) fluxes. *Front Physiol*. 2022;13:972104.
86 Cheng H, Fan C, Zhang SW, et al. Crystallization scale purification of alpha7 nicotinic acetylcholine receptor from mammalian cells using a BacMam expression system. *Acta Pharmacol Sin*. 2015;36(8):1013–1023.
87 Mehidi A, Rossier O, Schaks M, et al. Transient activations of Rac1 at the lamellipodium tip trigger membrane protrusion. *Curr Biol*. 2019;29(17):2852–28566.e5.
88 Hsia DA, Mitra SK, Hauck CR, et al. Differential regulation of cell motility and invasion by FAK. *J Cell Biol*. 2003;160(5):753–767.
89 Murphy DA, Courtneidge SA. The 'ins' and 'outs' of podosomes and invadopodia: characteristics, formation and function. *Nat Rev Mol Cell Biol*. 2011;12(7):413–426.
90 Berry CT, May MJ, Freedman BD. STIM- and Orai-mediated calcium entry controls NF-κB activity and function in lymphocytes. *Cell Calcium*. 2018;74:131–143.
91 Vig M, Kinet JP. Calcium signaling in immune cells. *Nat Immunol*. 2009;10(1):21–27.
92 Costantini TW, Coimbra R, Weaver JL, Eliceiri BP. CHRFAM7A expression in mice increases resiliency after injury. *Inflamm Res*. 2022;71(1):9–11.
93 Baird A, Coimbra R, Dang X, Eliceiri BP, Costantini TW. Up-regulation of the human-specific CHRFAM7A gene in inflammatory bowel disease. *BBA Clin*. 2016;5:66–71.
94 Courties A, Boussier J, Hadjadj J, et al. Regulation of the acetylcholine/alpha7nAChR anti-inflammatory pathway in COVID-19 patients. *Sci Rep*. 2021;11(1):11886.
95 Ramos FM, Delgado-Velez M, Ortiz AL, Baez-Pagan CA, Quesada O, Lasalde-Dominicci JA. Expression of CHRFAM7A and CHRNA7 in neuronal cells and postmortem brain of HIV-infected patients: considerations for HIV-associated neurocognitive disorder. *J Neurovirol*. 2016;22(3):327–335.
96 Courties A, Olmer M, Myers K, et al. Human-specific duplicate CHRFAM7A gene is associated with more severe osteoarthritis and amplifies pain behaviours. *Ann Rheum Dis*. 2023;82(5):710–718.
97 Bordas A, Cedillo JL, Arnalich F, et al. Expression patterns for nicotinic acetylcholine receptor subunit genes in smoking-related lung cancers. *Oncotarget*. 2017;8(40):67878–67890.